

## Quantitative investigation of gas flow, powder-gas interaction, and powder behavior under different ambient pressure levels in laser powder bed fusion

Xuxiao Li<sup>a</sup>, Qilin Guo<sup>b,c</sup>, Lianyi Chen<sup>b,c, \*\*</sup>, Wenda Tan<sup>a,\*</sup>

<sup>a</sup> Department of Mechanical Engineering, University of Utah, Salt Lake City, UT, 84124, USA

<sup>b</sup> Department of Mechanical Engineering, University of Wisconsin-Madison, Madison, WI, 53706, USA

<sup>c</sup> Department of Materials Science and Engineering, University of Wisconsin-Madison, WI, 53706, USA

### ARTICLE INFO

#### Keywords:

Laser powder bed fusion  
Gas flow  
Powder motion  
Multiphysics modeling  
High-speed X-ray imaging

### ABSTRACT

The powder motion in laser powder bed fusion (LPBF) processes causes defect and variability issues in the built products. It has been reported that the ambient pressure has a significant influence on the powder motion, but the physical effects of the ambient pressure on the gas flow, powder-gas interaction, and powder behavior are not quantitatively understood. In this work, we have developed the first three-dimensional multiphysics model for LPBF to simulate the molten pool dynamics, depression zone evolution, gas flow structure, and powder motion in a fully coupled manner. The model enables the first quantitative investigation of the gas flow, powder-gas interaction, and powder behavior in LPBF with different ambient pressure levels, all of which are difficult to measure by experiments. The simulation results show a consistent gas flow structure for all different pressure levels, but the gas flow parameters (temperature, velocity, Reynolds number, and Knudsen number) vary significantly with the ambient pressure. Four powder-gas interaction modes are defined by the gas flow around the particle and the gas-induced forces on the particle, and the interaction modes, individually or collectively, control the motion of each particle. With the changes in the ambient pressure and the gas flow parameters, the significance of the four modes to the powder motion varies, and the powder behavior (temperature, force, velocity, and ejection angle) becomes different. A new strategy is proposed to mitigate the powder motion based on the modeling results.

### 1. Introduction

Laser powder bed fusion (LPBF) is a mainstream additive manufacturing technology in which a laser selectively fuses metal powder particles layer-by-layer to print three-dimensional builds. Although LPBF has shown promising capabilities of achieving complex and flexible geometries to a designer's needs, there are defects and variability issues that inhibit further adaptation of this emerging manufacturing method. One major cause of the defects and print variability is the gas-flow-induced powder motion in LPBF. It has been reported in the literature that laser heating triggers strong evaporation on the metal surface. The vapor flux forms a vapor jet and entrains the surrounding gas, creating a complex gas flow, and eventually, the powder-gas interaction drives the powder motion [1]. It is observed that the powder particles have a tendency of being entrained towards and then ejected from the laser-illuminated zone (LIZ) [2,3]. The

entrainment dislocates the powder particles originally deposited around the LIZ [4]. The uniformity of the powder distribution is disrupted, which leads to the variability of builds from print to print. More importantly, the powder ejection gives rise to airborne spatters in solid or liquid form [5]. The spattering leads to a series of deleterious effects, including degraded surface roughness [6], lack-of-fusion [7], increased oxidation [8], and inhomogeneity of the feedstock [9], all of which contribute to poor mechanical properties in the final build [10].

Research efforts have been motivated to study the effects of process conditions on the powder motion in LPBF, in the hope that the powder motion can be mitigated, if not fully controlled. The investigated process conditions include varying the laser power and scanning speed [2,11], the ambient gas pressure [12–14] and composition [15,16], as well as applying a cross-flow in the build chamber [17]. Among these conditions, varying the ambient gas pressure is found to influence the powder motion dramatically. It is reported in Ref. [13] that the numbers of the entrained and ejected powder particles increase as the ambient pressure

\* Corresponding author. Department of Mechanical Engineering, University of Utah, Salt Lake City, UT, 84124, USA.

\*\* Corresponding author. Department of Mechanical Engineering, University of Wisconsin-Madison, Madison, WI, 53706, USA.

E-mail addresses: [lianyi.chen@wisc.edu](mailto:lianyi.chen@wisc.edu) (L. Chen), [wenda.tan@mech.utah.edu](mailto:wenda.tan@mech.utah.edu) (W. Tan).



Nomenclature	
$\rho$	: Density
$\vec{V}$	: Velocity
$t$	: Time
$p$	: Pressure
$\tau$	: Viscous stress
$\mu$	: Viscosity
$\vec{g}$	: Gravity
$\vec{S}_D$	: Darcy's term
$e$	: Total energy
$k$	: Thermal conductivity
$T$	: Temperature
$Y$	: Mass fraction of metal vapor
$D$	: Diffusivity of metal vapor
$K_D$	: Resistance function in Darcy's term
$\varphi$	: Levelset function
$\lambda$	: Mean free path
$R_s$	: Specific gas constant
$V_{ct}$	: Tangential velocity in the condensed phase
$V_{gt}$	: Tangential velocity in the gaseous phase
$\sigma_v$	: Tangential momentum accommodation coefficient
$m_p$	: Particle mass
$\vec{V}_{pc}$	: Velocity at particle center
$\vec{F}_f$	: Fluid-induced force on particle
$\vec{F}_{col}$	: Collision force on particle
$I_p$	: Moment of inertia of particle
$\vec{\omega}_p$	: Angular velocity of particle
$\alpha_k$	: Spring coefficient for particle collision
$\alpha_d$	: Damping coefficient for particle collision
$E$	: Young's modulus
$\nu$	: Poisson's ratio
$\zeta$	: Damping coefficient

is decreased below the atmospheric pressure (1 bar). Under extremely low ambient pressure (smaller than 1 mbar), few particles can be entrained near the LIZ, and the particles surrounding the LIZ are mostly ejected. Similar observations are reported in Ref. [12] where the authors correlate the ambient pressure with the vapor jet divergent angle and the powder motion. Apparently, extremely low ambient pressure leads to a large amount of ejected powder particles and therefore should be avoided. The authors in Ref. [18] explored the window of ambient pressure between 10 mbar and 1 bar and found that 200 mbar achieves a similar amount but less variability of spattered particles. For the ambient pressure higher than the atmospheric pressure, the only study found in the literature is [14]. This rareness might be explained by the difficulty of building a high-pressure chamber. According to Ref. [14], the number of entrained particles is decreased as the ambient pressure is increased above 1 bar, but the number of ejected particles is increased. The authors suggested that high ambient pressure does not have an advantage in reducing the powder motion.

There is a large parameter window (laser power, scanning speed, ambient pressure, etc.) from which one can identify the optimal parameter combinations to mitigate the powder motion. In that regard, the underlying physics of the powder-gas interaction needs to be fully understood to minimize the costly trial-and-error tests to identify the optimal conditions. The high-speed X-ray and optical imaging are capable of visualizing and tracking the powder motion with high spatial (up to 1  $\mu\text{m}$ ) and temporal resolution (up to 1  $\mu\text{s}$ ). However, quantitative information regarding the powder-gas interaction, i.e., the gas flow surrounding the powder particles and the forces exerted on the particle surfaces, is difficult to measure experimentally. In this regard, multiphysics simulations can be a complement to the imaging techniques to determine these quantities.

Multiphysics simulations have been extensively utilized to study the molten pool behavior in LPBF. The simulated phenomena include the laser-metal interaction [7], molten pool flow [19,20], pore formation [21,22], keyhole instability [23], balling [24], and lack-of-fusion development [25,26]. There are relatively fewer efforts for gas flow simulations in LPBF. The vapor jet expansion and the entrainment flow were simulated in Ref. [2] but the thermal-fluid coupling between the gas and the molten pool was ignored. This coupling was added in a later study [27], but the simulation did not track the powder motion. Powder particles are typically either ignored or assumed to be sintered to the substrate. In a recent publication [28], the gas flow and powder motion were simulated, but the gas flow was decoupled with the molten pool dynamics. The vapor jet was artificially defined, and the effects of the jetting angle on the powder motion were investigated. In a previous

publication [29], we developed a two-dimensional (2D) model that fully coupled the molten pool dynamics, gas flow, and powder motion. However, the phenomena in the third dimension were ignored, which can compromise the fidelity of the simulation results.

In an attempt to further improve the fidelity of multiphysics simulations, we extend our previous 2D model to a three-dimensional (3D) model in this work. Particularly, the 3D model is used to investigate the effects of the ambient pressure on the gas flow, powder-gas interaction, and powder behavior. The simulation results are validated against high-speed X-ray imaging experiments. The model predictions of gas pressure, velocity, and temperature, as well as the powder quantities such as force, velocity, and temperature, are identified as functions of the ambient pressure, which are used to quantitatively understand the underlying physics under different ambient pressure levels.

## 2. Methods

### 2.1. Multiphysics simulation

The calculation domain for the multiphysics simulation consists of the condensed phase region and the gaseous phase region. The condensed region includes the substrate, molten pool, and the individual powder particles. The gaseous region includes the metal vapor due to evaporation and the ambient protection gas (typically argon). The interface between the condensed and gaseous region is referred to as the C-G interface. The calculation domain is discretized into a Cartesian mesh, and variables are computed at each cell of the mesh using computational fluid dynamics (CFD) methods. Both the condensed and gaseous regions are subject to CFD computation. The C-G interface is captured by the level-set method. The individual particles are tracked by the discrete element method (DEM). The CFD and DEM computations are fully-coupled and carefully coordinated to model the powder-gas interaction. The modeling methodology of the current model is consistent with our previous model, with the dimension extended from 2D to 3D. The methods are briefly described here, and more details can be referred to Refs. [29–32].

The governing equations for the CFD computation are the conservation equations of mass, momentum, energy, and the vapor species:

$$\frac{\partial \rho}{\partial t} + \nabla \cdot (\rho \vec{V}) = 0 \quad (1)$$

$$\frac{\partial(\rho V)}{\partial t} + \nabla \cdot (\rho \vec{V} \vec{V}) = -\nabla p + \nabla \cdot \tau + \rho \vec{g} + \vec{S}_D \quad (2)$$

$$\frac{\partial(\rho e)}{\partial t} + \nabla \cdot (\rho e \vec{V}) = -\nabla \cdot (p \vec{V}) + \nabla \cdot (\tau \cdot \vec{V}) + \rho \vec{g} \cdot \vec{V} + \nabla \cdot (k \nabla T) \quad (3)$$

$$\frac{\partial(\rho Y)}{\partial t} + \nabla \cdot (\rho Y \vec{V}) = \nabla \cdot (\rho D \nabla Y) \quad (4)$$

Here, Eq. (1) is the mass conservation equation where  $\rho$  is the density,  $\vec{V}$  is the velocity, and  $t$  is the time. Eq. (2) is the momentum conservation equation where  $p$  is the pressure,  $\tau$  is the viscous stress tensor,  $\vec{g}$  is the gradational vector, and  $\vec{S}_D$  is the Darcy's term. Eq. (3) is the energy conservation equation where  $e$  is the total energy (internal and kinetic energy), and  $k$  is the thermal conductivity. Eq. (4) is the vapor species conservation equation where  $Y$  is the mass fraction of the metal vapor in the gaseous region, and  $D$  is the diffusion coefficient of the vapor. It is assumed that the condensed region is a continuum with only one species (metal), and the gaseous region has two species, metal vapor and argon gas. Eq. (4) is only solved in the gaseous region. The Darcy's term is written as:

$$S_D = -K_D(T) \left( \vec{V} - \vec{V}_s \right) \quad (5)$$

In Eq. (5),  $\vec{V}_s$  is a solid velocity. It is assigned to be the particle velocity if the cell is inside a powder particle, and is assigned to be zero otherwise.  $K_D$  is a function of temperature  $T$ . It is a large number if  $T$  is below the solidus temperature, is equal to zero if  $T$  is above the liquidus temperature, and is smoothly connected if  $T$  is in between. With Eqs. (1)–(4), the pressure, velocity, temperature, and vapor mass fraction can be obtained at each cell center by the CFD computation.

The evolution of the C-G interface is governed by the level-set advection equation:

$$\frac{\partial \varphi}{\partial t} + \vec{V} \cdot \nabla \varphi = 0 \quad (6)$$

In Eq. (6),  $\varphi$  is the level-set function.  $\varphi$  is defined to be the signed distance to the interface, and the zero-level-set isosurface represents the C-G interface. Once the C-G interface is identified, the ghost fluid method is applied to separate the calculation domain into the condensed and gaseous region. The boundary conditions are carefully defined at the C-G interface to capture the interface phenomena, including the surface tension, thermal-capillary (Marangoni) effect, recoil pressure, and evaporation vapor flux.

Different from our previous model, a slip boundary condition is implemented in the current model to adapt for the larger Knudsen number in the gas that may occur in the low ambient pressure condition. The Knudsen number is defined as the ratio of the mean free path  $\lambda$  to a physical length scale  $L$ :  $Kn = \lambda/L$ . Here,  $L$  can be a typical powder diameter in LPBF. The mean free path  $\lambda$  is calculated as:

$$\lambda = \frac{\mu}{\rho} \sqrt{\frac{\pi}{2R_s T}} \quad (7)$$

In Eq. (7),  $\mu$  is the gas viscosity, and  $R_s$  is the specific gas constant. The Knudsen number can be used as the criterion to classify the "flow regimes" as follows [33,34]:

- $0 \leq Kn \leq 0.01$ : continuum flow (Navier-Stokes equation with no-slip boundary condition).
- $0.01 \leq Kn \leq 0.1$ : slip flow (Navier-Stokes equation with slip boundary condition).
- $Kn \geq 0.2$ : Navier-Stokes equation should be replaced with the Boltzmann equation (statistical mechanics).

As will be presented later, the Knudsen number in the gaseous region is typically  $>0.01$  when the ambient pressure is lower than 1 bar. Under this Knudsen number, the flow can enter the "slip flow" regime, and the slip boundary condition needs to be applied. Under extremely low pressure, the Knudsen number is  $> 0.2$ . This flow regime is beyond the

capability of the current "continuum flow" model described by Eqs. (1)–(4). Therefore, only ambient pressure larger than 10 mbar is simulated (discussed later). The slip boundary condition can be written as:

$$V_{ct} - V_{gt} = \frac{2 - \sigma_v}{\sigma_v} \lambda \frac{\partial V_{gt}}{\partial n} \quad (8)$$

In Eq. (8),  $V_{ct}$  and  $V_{gt}$  are the tangential velocity on the condensed and gaseous side of the C-G interface, and their difference is the velocity slip.  $\sigma_v$  is the tangential momentum accommodation coefficient.  $(\partial V_{gt}/\partial n)$  is the gradient of  $V_{gt}$  along the normal direction  $n$  of the C-G interface.

In the DEM computation, the initial powder bed configuration is randomly generated by a rain-dropping algorithm [35]. Then, the motion of each powder particle is tracked according to the Newton's equations of motion:

$$m_p \frac{d\vec{V}_{pc}}{dt} = \oint_{S_p} \vec{F}_f dS + m_p \vec{g} + \vec{F}_{col} \quad (9)$$

$$I_p \frac{d\vec{\omega}_p}{dt} = \oint_{S_p} \vec{r} \times \vec{F}_f dS \quad (10)$$

In Eqs. (9) and (10),  $m_p$  is the mass of the particle,  $\vec{V}_{pc}$  is the velocity at the particle center,  $I_p$  is the moment of inertia of the particle, and  $\vec{\omega}_p$  is the angular velocity of the particle. The integrations on the right-hand-side of Eqs. (9) and (10) are carried out on the particle surface  $S_p$ .  $\vec{F}_f$  is the force exerted by the surrounding flow on  $S_p$ , which can be obtained from the CFD computation.  $\vec{r}$  is a vector pointing from the particle center to the particle surface.  $\vec{F}_{col}$  is the force resulted from the collision with surrounding particles. The force exerted on the  $i$ th particle by its collision with the  $j$ th particle can be calculated as:

$$F_{col,ij} = -(\alpha_{k,ij} \delta_{ij} + \alpha_{d,ij} V_{n,ij}) n_{ij} \quad (11)$$

In Eq. (11),  $n_{ij}$  is a unit vector pointing from the  $i$ th particle to the  $j$ th particle.  $\delta_{ij}$  is the gap between the two particles calculated by  $\delta_{ij} = R_i + R_j - d_{ij}$ , where  $R_i$  and  $R_j$  are the radii of the  $i$ th and  $j$ th particles, and  $d_{ij}$  is the distance between the two particles. The collision force in Eq. (11) is only activated when the gap  $\delta_{ij}$  is negative, i.e., there is an overlap between the two particles. Otherwise,  $F_{col,ij}$  is set to be zero.  $V_{n,ij}$  is the normal relative velocity of the  $i$ th particle with respect to the  $j$ th particle, calculated as  $V_{n,ij} = (V_i - V_j) \cdot n_{ij}$ , where  $V_i$  and  $V_j$  are the velocities at the center of the  $i$ th and the  $j$ th particles.  $\alpha_{k,ij}$  and  $\alpha_{d,ij}$  are the spring and damping coefficient for the collision, calculated by:

$$\alpha_{k,ij} = \left( \frac{8}{15} \right)^{0.8} \left[ \left( \frac{R_i R_j}{R_i + R_j} \right)^2 \frac{m_i m_j}{m_i + m_j} \left( \frac{E}{1 - \nu^2} \right)^4 \nu^2 \right]^{0.2} \quad (12)$$

$$\alpha_{d,ij} = 2m_i \zeta \sqrt{\frac{\alpha_{k,ij}}{m_i}} \quad (13)$$

In Eqs. (12) and (13),  $m_i$  and  $m_j$  are the mass of the  $i$ th and the  $j$ th particle.  $E$  is the Young's modulus of the metal,  $\nu$  is the Poisson's ratio, and  $\zeta$  is the damping ratio.

In all the simulations and experiments of this work, the powder and substrate material is stainless steel 316 L, and the ambient gas material is argon. Their thermophysical properties used in the CFD and DEM computation are listed in Table 1. The calculation domain and mesh of the simulation are shown in Fig. 1. A fine-mesh region (Fig. 1(a)) is defined to capture the major physical phenomena, e.g., the molten pool dynamics and the powder-gas interaction. A uniform mesh size of 5 μm is used for the fine mesh. Coarse mesh is extended from the fine-mesh region along all ± X, ± Y, and ± Z directions, as shown in Fig. 1(b). The purpose of the coarse mesh is to allow the gas flow to be fully developed within the calculation domain.

**Table 1**

Thermophysical properties of stainless steel 316 L and argon gas [36–39].

Property	Stainless Steel 316 L			Argon
	Solid	Liquid	Vapor	
Density ( $\text{kg m}^{-3}$ )	T dependent	T dependent	Ideal gas	Ideal gas
Phase change temperature (K)	1675 (solidus)	1708 (liquidus)	3135 (boiling)	–
Specific heat ( $\text{J kg}^{-1} \text{ K}^{-1}$ )	847	714	495	520
Phase change latent heat ( $\text{J kg}^{-1}$ )	–	$2.9 \times 10^5$ (melting)	$7.45 \times 10^6$ (vaporization)	–
Thermal conductivity ( $\text{W m}^{-1} \text{ K}^{-1}$ )	T dependent	T dependent	T dependent	T dependent
Viscosity ( $\text{kg m}^{-1} \text{ s}^{-1}$ )	–	0.015	T dependent	T dependent
Surface tension ( $\text{N m}^{-1}$ )	–	$1.7\text{--}1.5 \times 10^{-4} \text{ T}$	–	–
Young's Modulus (MPa)	$2.2 \times 10^3$			
Poisson's ratio	0.3			
Damping ratio	0.5			
Tangential momentum accommodation coefficient			1.0	

## 2.2. High-speed X-ray imaging

High-speed synchrotron X-ray imaging experiment is performed for in-situ observation of the powder motion during LPBF under various ambient pressure levels. The synchrotron X-ray beam is provided by the 32-ID-B beamline of the Advanced Photon Source (APS), Argonne National Laboratory (ANL). The detailed information about the setup for in-situ X-ray imaging of LPBF has been documented in Ref. [12]. In brief, a miniature stainless steel 316 L powder bed is assembled with a metal plate (substrate) sandwiched by two glassy carbon plates, which are used to contain the powder layer on top of the substrate. The powder layer is spread manually with  $100 \pm 10 \mu\text{m}$  thickness. The width of the powder bed (the distance between two glassy carbon plates) is  $500 \mu\text{m}$ .

We note that a larger sample width will reduce the X-ray imaging visibility of the powder bed, while a smaller sample width makes the experiment deviate too much from a real LPBF process. The visibility of DZ is sacrificed in the current experiment, as a clear observation of DZ requires a much smaller sample width. A laser beam, with  $1070 \pm 10 \text{ nm}$  wavelength and  $\sim 200 \mu\text{m } 1/e^2$  beam diameter, is used to melt the powder bed from above. The laser output is 312 W in power and 800  $\mu\text{s}$

in duration in the present work. The laser beam is kept stationary to realize a “spot welding” type of laser melting. The powder particles have a mean diameter of  $40 \mu\text{m}$ . The synchrotron X-ray beam penetrates and illuminates the laser-matter interaction region from the horizontal direction. The transmitted X-ray is converted into visible light by a LuAG: Ce scintillator, and then recorded by a high-speed visible-light camera (Photron FastCam SA-Z). The powder bed is enclosed in a vacuum chamber, refilled with high purity argon gas to adjust the inner chamber pressure.

## 3. Result and discussion

Simulations and experiments are utilized simultaneously to investigate the effects of ambient pressure. Different ambient pressure levels are used in the investigation, as summarized in Table 2. Four ambient pressure levels in the atmospheric and sub-atmospheric (sub-atm) conditions (1 bar, 400 mbar, 50 mbar, 10 mbar) are investigated in both simulations and experiments. Hyper-atmospheric (hyper-atm) conditions are not investigated with experiments due to the difficulties of building a high-pressure chamber, but two hyper-atm pressure levels (3 bar, 5 bar) are investigated using simulations. Extremely low pressure levels ( $< 10 \text{ mbar}$ ) are not investigated in the current work because the Knudsen number is typically  $> 0.2$ , as discussed earlier. The current work will focus on the pressure range 10 mbar–5 bar. For each pressure level in Table 2, at least three experiments and simulations are conducted with random initial configurations of the powder bed to ensure the statistical reliability of the results.

### 3.1. Overview of simulation and experimental results

Exemplary results from the 3D simulation are shown in Fig. 2. The corresponding animations are given in Supplementary Video 1. A time sequence is presented in Fig. 2(a–e) to demonstrate the dynamic process. A variety of quantitative information, not directly measurable from the experiment, can be extracted from the simulation. Fig. 2(a and b) shows the laser absorption distribution and temperature field on the C-G interface. A vertical slice is extracted to show the gas flow in Fig. 2(c–e),

**Table 2**  
Ambient pressure levels investigated.

Pressure group	Pressure Level	Investigation approach
Low pressure	10 mbar, 50 mbar	Experiment & Simulation
Medium pressure	400 mbar, 1 bar	Experiment & Simulation
High pressure	3 bar, 5 bar	Simulation

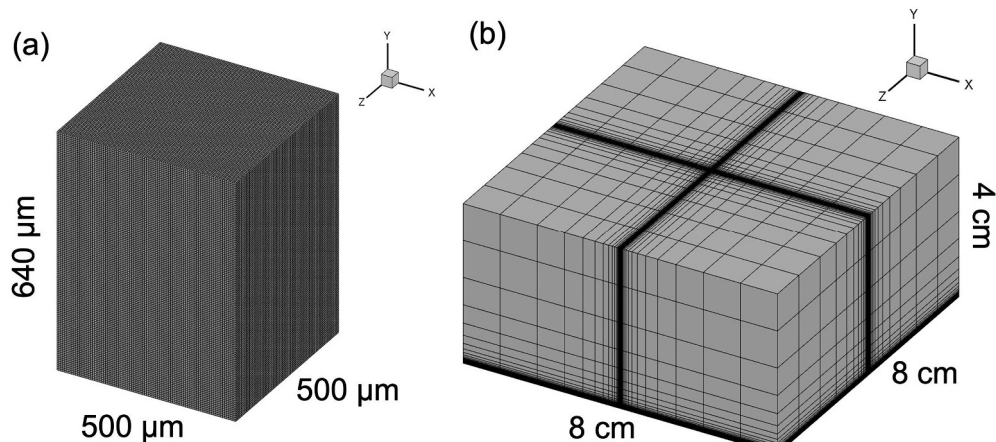


**Fig. 1. Simulation domain and mesh.** (a) Fine mesh region with a uniform mesh size of  $5 \mu\text{m}$ . (b) Entire calculation domain showing the coarse mesh extended from the fine mesh.

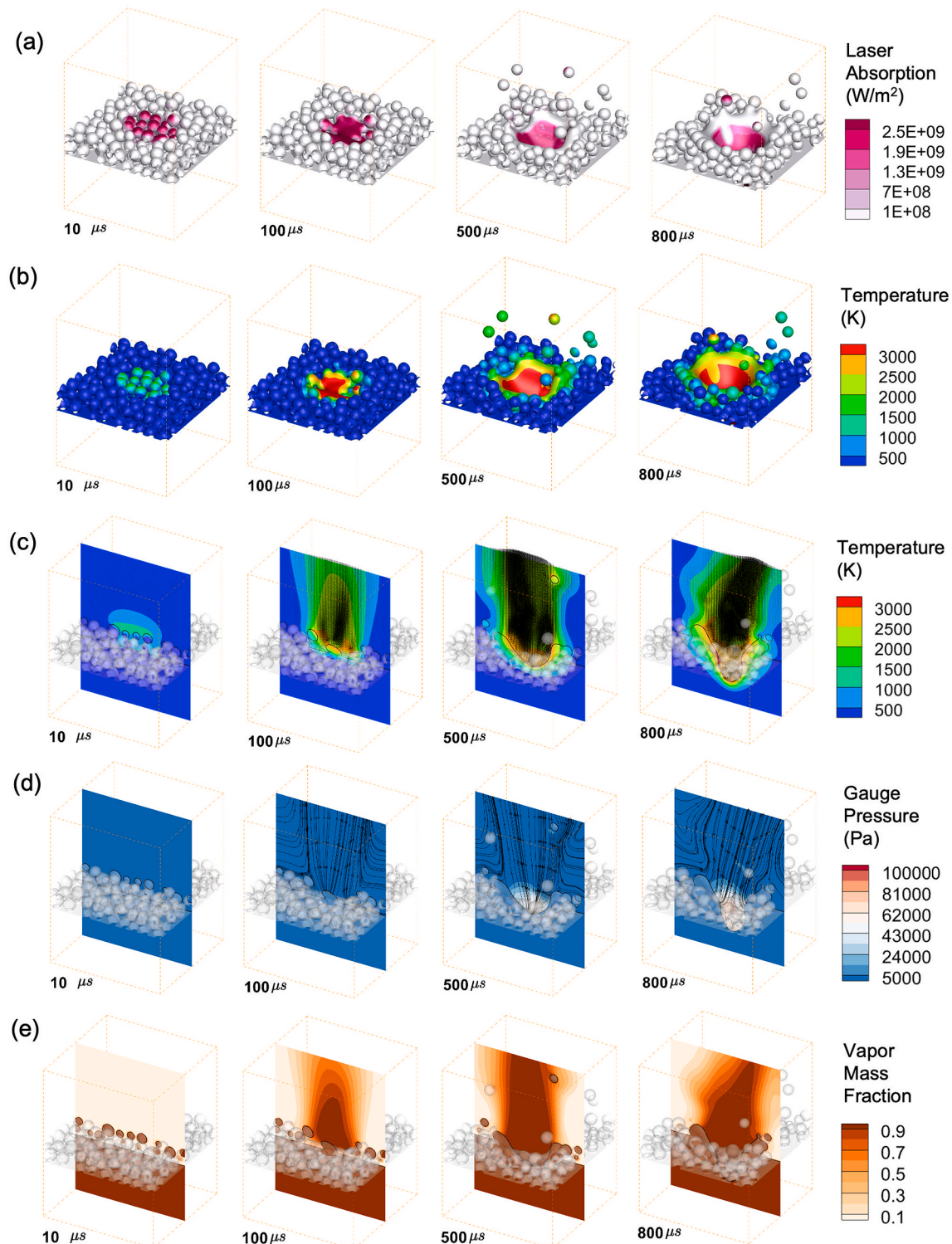


**Fig. 2. Demonstration of the 3D model.** A time sequence is selected from the simulation for  $p_{amb} = 400$  mbar. The timestamp indicates the time period since the laser is turned on. (a) Laser absorption on the C-G interface. (b) The temperature on the C-G interface. (c) Vertical slice showing the temperature and flow field in the gaseous region. (d) Vertical slice showing the gauge pressure and streamlines of the flow in the gaseous region. (e) Vertical slice showing the vapor mass fraction field in the gaseous region.

where the temperature, velocity, (gauge) pressure, and vapor mass fraction field can be quantified. The gauge pressure is defined as the difference between absolute and ambient pressure,  $p - p_{amb}$ . The laser heating of the powder bed, shown by Fig. 2(a), results in the powder melting, formation of the depression zone (DZ), and the powder motion (Fig. 2(b)). It can be seen in Fig. 2(c, e) that the evaporation occurs at the

molten pool surface, causing the formation of the DZ and vapor jet. The vapor jet induces the entrainment of the surrounding gas, as shown by the streamlines in Fig. 2(d). Both the vapor jet and the entrainment flow contribute to the powder motion. These pieces of quantitative information will be examined thoroughly in later discussions.

Supplementary data related to this article can be found online at

<https://doi.org/10.1016/j.ijmachtools.2021.103797>

To validate the current model, we compare between experiment and simulation results at the pressure levels (1 bar, 50 mbar, 10 mbar) in Fig. 3(a–c). The animations for Fig. 3(a), (b), and Fig. 3(c) are given as Supplementary Video 2, 3, and 4, respectively. As the ambient pressure decreases, there are more spattered powder particles and the diverging angle of ejection increases. These observations agree with the results in Ref. [12]. We compared the velocity of the ejected particles between experiment and simulation results at each pressure level, as shown in Fig. 4. Here, we extracted the maximum velocity during the lifespan of each ejected particle and presented the average and extreme values over all the ejected particles with the error bars in Fig. 4. The magnitude of the particle velocity matches reasonably well between simulation and experiment.

Supplementary data related to this article can be found online at <https://doi.org/10.1016/j.ijmachtools.2021.103797>

It is noticed that the ejected particles can be in a liquid form. These liquid particles can deform and attach to other particles to form clusters, as seen in the X-ray imaging results in Fig. 3. In the current model, the particles are assumed as rigid bodies as a simplification. The temperature distribution in the particle (as shown in the simulations in Fig. 3) is computed, but the fluid flow inside the particle is ignored. Thus, the particles do not deform or cluster in the simulation when the temperature goes above the liquidus temperature.

In the following discussion, the gas flow as a function of ambient pressure is first analyzed. After that, the powder motion driven by the powder-gas interaction are analyzed under different ambient pressure levels. Finally, we track the powder particles in all the simulations and statistically quantify the powder behavior, such as the velocity, forces, and temperature of the particles.

### 3.2. Vapor jet and induced entrainment flow

Significant gas flow occurs when the vapor jet initiates from the molten pool surface. The vapor jet then induces the entrainment of the ambient gas. The formation and development of the vapor jet at different ambient pressure levels are examined in Fig. 5. (5 bar, 1 bar, 10 mbar) are selected as the representative levels for the high-, medium-, and low-pressure groups in Table 2. In Fig. 5, a vertical slice with the temperature and flow field is extracted (as in Fig. 2(c)) at four moments to characterize the key physical events.

It is observed in Fig. 5(a–c) that the evaporation initiates about 40–70  $\mu$ s after the laser is turned on, which agrees with the observation in Ref. [12]. With the decrease of ambient pressure, the evaporation starts earlier because the boiling temperature is lower under lower pressure. According to the Clausius-Clapeyron equation, the boiling temperature is about 2350 K, 3150 K, and 3550 K under ambient pressure levels 10 mbar, 1 bar, and 5 bar, respectively. At about 80–90  $\mu$ s, the powder particles merge into a molten pool, and a vapor jet emerges from the molten pool surface. After that, the vapor jet develops as the recoil pressure on the molten pool surface creates the DZ. At the last moment in Fig. 5(a–c), the vapor jet has reached a “stable” state, where the temperature and flow field do not significantly change with time.

Fig. 5 shows that the temperature in the vapor jet is significantly decreased as the ambient pressure decreases. The stable vapor jet temperature at the opening of DZ is about 3400 K, 2700 K, and 2100 K, for  $p_{amb}$  = 5 bar, 1 bar, and 10 mbar, respectively. This can be again explained by the lower boiling temperature under lower pressure. For the flow field, it can be observed that the vapor jet is confined and has a small velocity under high ambient pressure (Fig. 5(a)). As the ambient pressure decreases, the vapor jet expands more freely and has an increasingly larger velocity (Fig. 5(b and c)).

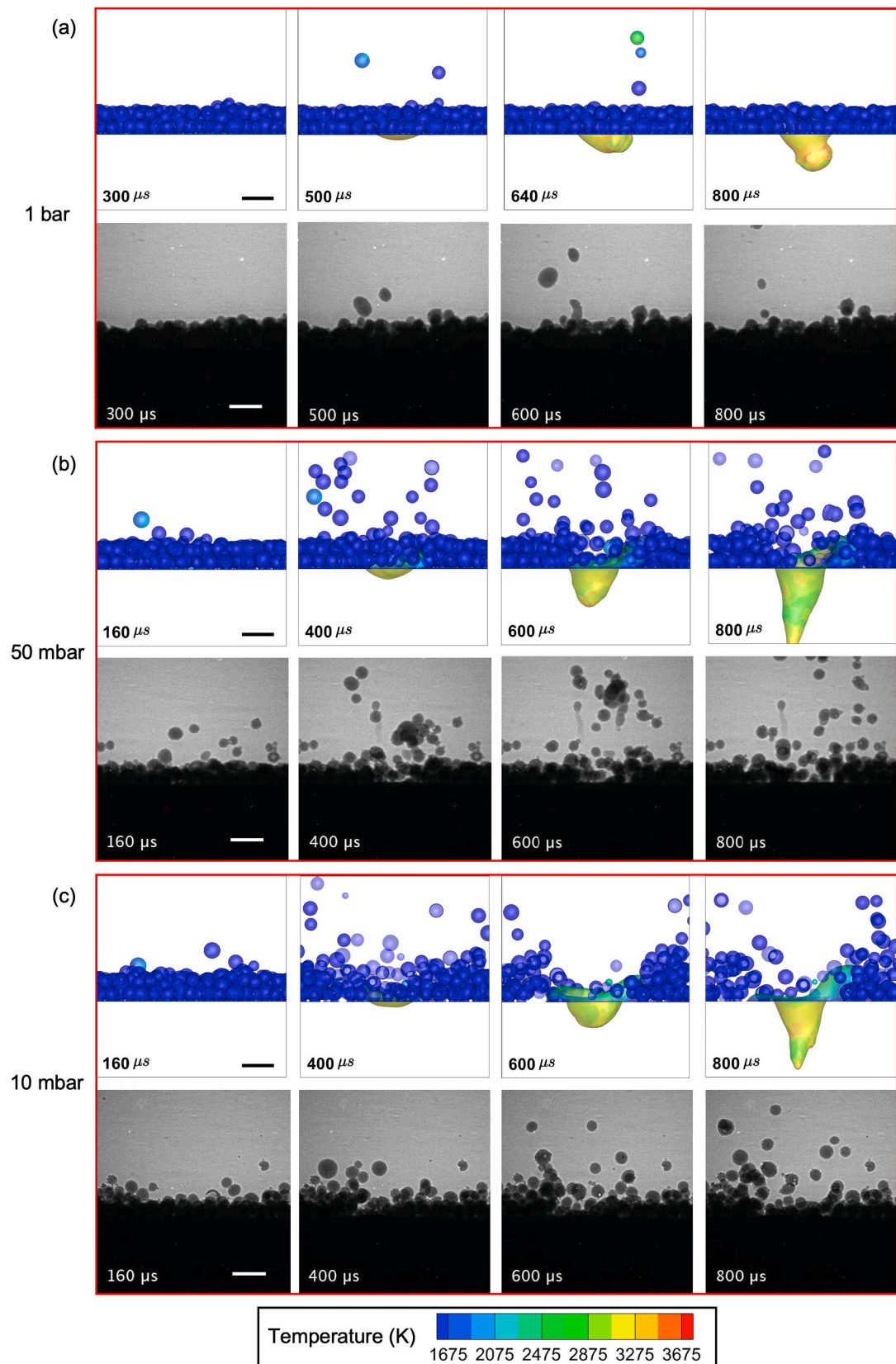
To further analyze the structure of the vapor jet and induced entrainment flow, we extract more quantitative information at the last moment in Fig. 5(a–c) when the vapor jet has reached the stable state, as detailed in Fig. 6. The velocity magnitude in a vertical slice is shown in

Fig. 6(a), which is at the same slicing location as in Fig. 5. The pressure field and streamlines for the vertical slice are shown in Fig. 6(b). To characterize the three-dimensional flow field, we extract a horizontal slice cutting through the powder bed. The projected (horizontal) velocity magnitude is shown in Fig. 6(c). The pressure field and streamlines for the horizontal slice is shown in Fig. 6(d). The dashed circle in Fig. 6(c and d) marks the LIZ. We will use Fig. 6(a and b) to characterize the vapor jet expansion and Fig. 6(c and d) to characterize the induced entrainment flow.

For all the ambient pressure levels, the vapor jet expansion is driven by the pressure decrease from the DZ bottom towards the DZ opening, as shown in Fig. 6(b). The pressure decrease corresponds to an increase of velocity magnitude from the DZ bottom towards the DZ opening (Fig. 6(a)). The velocity reaches its maximum at a location above the DZ where the pressure does not notably change anymore along the streamlines. Then, the velocity magnitude decreases radially towards the ambient as the vapor jet momentum dissipates into its surrounding. We denote the pressure difference between the DZ bottom and DZ opening in Fig. 6(b) as  $\Delta p_{exp}$ , which can be viewed as the driving force for the vapor jet expansion.  $\Delta p_{exp}$  is relatively small ( $\sim 10^4$  Pa) under high ambient pressure (5 bar), which corresponds to a weak vapor jet expansion. Under 1 bar,  $\Delta p_{exp}$  is increased to  $\sim 10^5$  Pa. As the ambient pressure further decreases to  $10^3$  Pa,  $\Delta p_{exp}$  does not significantly change, but the vapor jet expands with a larger diverging angle due to the less confinement imposed by the small ambient pressure. The Bernoulli equation for the compressible flow can be written as  $\frac{1}{2}\rho v^2 + \frac{\gamma}{\gamma-1}p = constant$ , where  $\rho$  is the density,  $v$  is the streamline-wise velocity,  $\gamma$  is the specific heat ratio, and  $p$  is the pressure. As the pressure decreases from the DZ bottom to the DZ opening (by  $\Delta p_{exp}$ ), the momentum  $\rho v^2$  increases according to the Bernoulli equation. With the pressure decrease  $\Delta p_{exp}$  being similar ( $\sim 10^5$  Pa) for the cases of  $p_{amb}$  = 1 bar and  $p_{amb}$  = 10 mbar, the increase of momentum  $\rho v^2$  should also be comparable in these two cases. Since  $\rho$  is significantly smaller for  $p_{amb}$  = 10 mbar, the velocity increase is significantly larger. To summarize, the vapor jet velocity is expected to increase as the ambient pressure decreases, which is confirmed in Fig. 6(a). The vapor jet expansion velocity,  $V_{exp}$ , can be characterized by the maximum velocity in the vapor jet.  $V_{exp}$  is plotted as a function of  $p_{amb}$  in Fig. 5(a) where  $V_{exp}$  is about 200 m/s, 1000 m/s, and 1500 m/s for  $p_{amb}$  = 5 bar ( $5 \times 10^5$  Pa), 1 bar ( $1 \times 10^5$  Pa), and 10 mbar ( $1 \times 10^3$  Pa), respectively.

The induced entrainment flow is visualized by the streamlines in Fig. 6(d). For all ambient pressure levels, a high-pressure region is formed in the LIZ (dashed circle), where the vapor jet is initiated. Right outside the high-pressure region, there is a “ring” of low-pressure region beyond which the pressure is close to the ambient pressure. The low-pressure ring acts as a separation between the entrained gas and the expanding vapor. Outside the “ring,” the gas is driven towards the LIZ by the pressure difference between the “ring” and ambient. Inside the ring, the gas radially expands from the LIZ outwards. We denote the pressure difference between the ambient and the low-pressure ring as  $\Delta p_{etr}$ , which can be viewed as the driving force for the entrainment flow.  $\Delta p_{etr}$  is relatively small ( $\sim 100$  Pa) under high ambient pressure (5 bar), indicating weak entrainment. At 1 bar,  $\Delta p_{etr}$  is increased to  $\sim 500$  Pa.  $\Delta p_{etr}$  does not significantly change as the ambient pressure further decreases to 10 mbar, but the size of the low-pressure ring is significantly increased due to the enhanced vapor jet expansion. Again, according to the Bernoulli equation,  $\Delta p_{etr}$  can cause larger entrainment velocity under low ambient pressure. As confirmed in Fig. 6(c), the entrainment velocity is increased as the ambient pressure decreases. The entrainment velocity,  $V_{etr}$ , can be characterized by the projected velocity at the outer edge of the low-pressure ring.  $V_{etr}$  is plotted as a function of  $p_{amb}$  in Fig. 5(a) where  $V_{etr}$  is  $\sim 5$  m/s, 20 m/s, and 50 m/s for  $p_{amb}$  = 5 bar ( $5 \times 10^5$  Pa), 1 bar ( $1 \times 10^5$  Pa), and 10 mbar ( $1 \times 10^3$  Pa), respectively.

Finally, we quantify the Reynolds number (Re) and Knudsen number ( $Kn$ ) for the gas flow as functions of ambient pressure, as shown in Fig. 7



**Fig. 3. Powder motion from the simulation and X-ray imaging.** (a)  $p_{amb} = 1$  bar. (b)  $p_{amb} = 50$  mbar. (c)  $p_{amb} = 10$  mbar. The timestamp indicates the time period since the laser is turned on. All the scale bars are 100  $\mu m$ . The simulation results are shown from a projected view similar to that in X-ray imaging experiments. The temperature is shown on the C-G interface for the simulation.

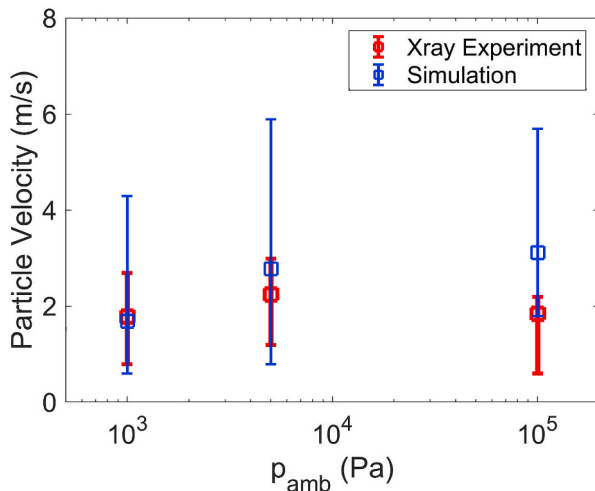


**Fig. 4.** Comparison of velocity for the ejected particles between X-ray experiment and simulation.

(b and c). The Reynolds number is defined as  $Re = \rho UL / \mu$ , where  $\rho$  is the gas density,  $U$  is the velocity magnitude,  $\mu$  is the gas viscosity, and  $L$  is a physical length scale chosen to be 50  $\mu\text{m}$  as the typical diameter of a large powder particle. The Knudsen number is again defined as  $Kn = \lambda /$

$L$ . The Reynolds number is considered as the ratio between the inertia and viscous force and has been used to estimate the drag force exerted by the gas flow on powder particles [1,28]. The Knudsen number, as discussed earlier, can be used to judge whether statistical mechanics or (continuum) fluid dynamics governs the flow behavior. We select two locations in the horizontal slice in Fig. 6(c and d) to characterize  $Re$  and  $Kn$  of the gas flow. The first location is the center of the LIZ, which is considered the typical location where the powder particles are ejected. The second location is a typical location on the outer edge of the low-pressure ring, where powder particles are subjected to the entrainment flow. These two locations are denoted as “jet center” and “jet edge,” and their ( $Re$ ,  $Kn$ ) values are calculated from simulations and shown in Fig. 7(b and c).

It is observed in Fig. 7(b) that the Reynolds number does not vary notably for the high and medium pressure levels (5 bar and 1 bar).  $Re$  is  $\sim 100$  at the jet center and  $\sim 10$  at the jet edge. Under low ambient pressure (10 mbar),  $Re$  decreases to  $\sim 50$  at the jet center and  $\sim 1$  at the jet edge. The decrease of  $Re$  can be attributed to the small gas density due to the low ambient pressure. It is also noted that the Reynolds number is typically 1–2 magnitudes smaller at the jet edge than the jet center. The drag force on powder particles can be estimated using the “Stokes limit” assumption [1], which assumes that the Reynolds number approaches zero. We point out that the Stokes limit assumption can be justified for the entrainment flow around the powder particles as  $Re \leq 10$ . However, the Reynolds number is  $\sim 100$  for the surrounding gas flow when powder particles are ejected. In such a case, the Stokes limit

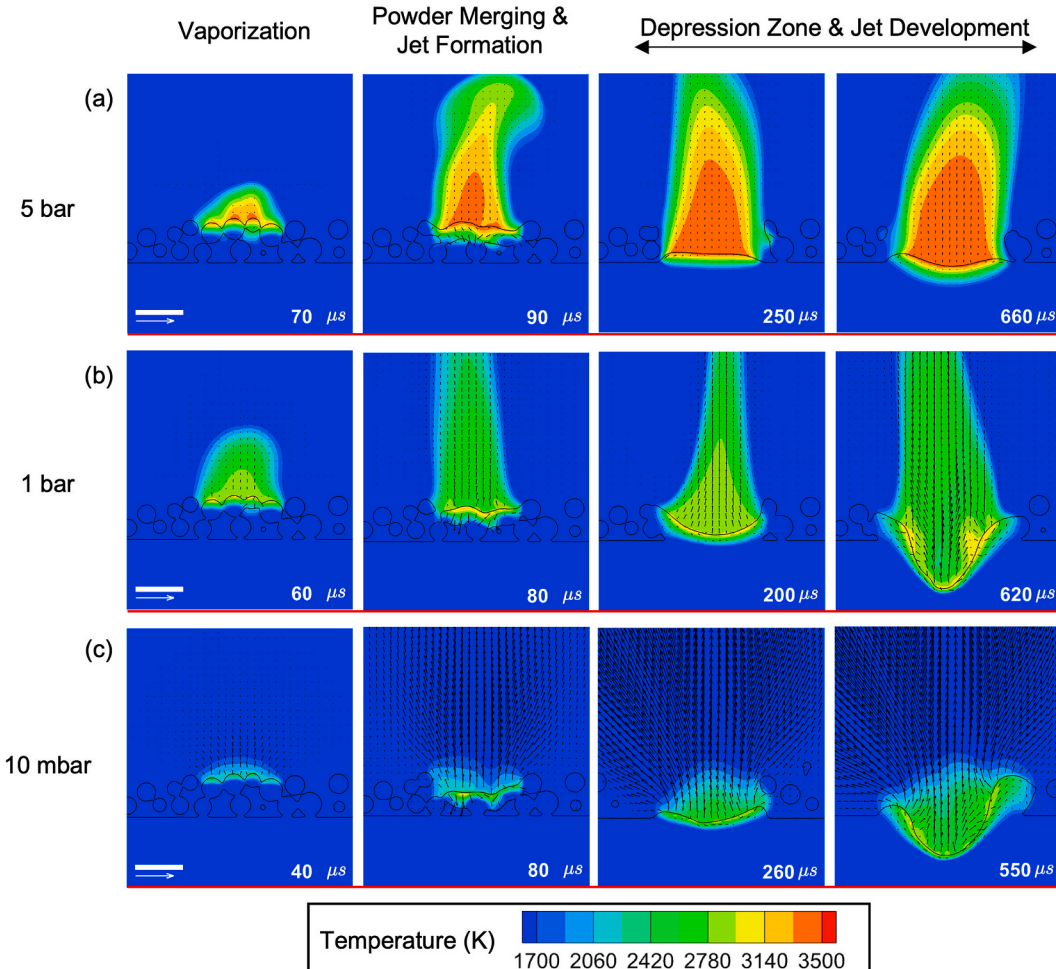


**Fig. 5.** Vapor jet formation and development under different ambient pressure levels. (a)  $p_{amb} = 5$  bar. (b)  $p_{amb} = 1$  bar. (c)  $p_{amb} = 10$  mbar. For (a–c), a time sequence is given to characterize the key physical events. The vertical slice is at the same location shown in Fig. 2(c and d). All scale bars are 100  $\mu\text{m}$ . All arrow keys are 2000 m/s in the gaseous region and 8 m/s for the condensed region.

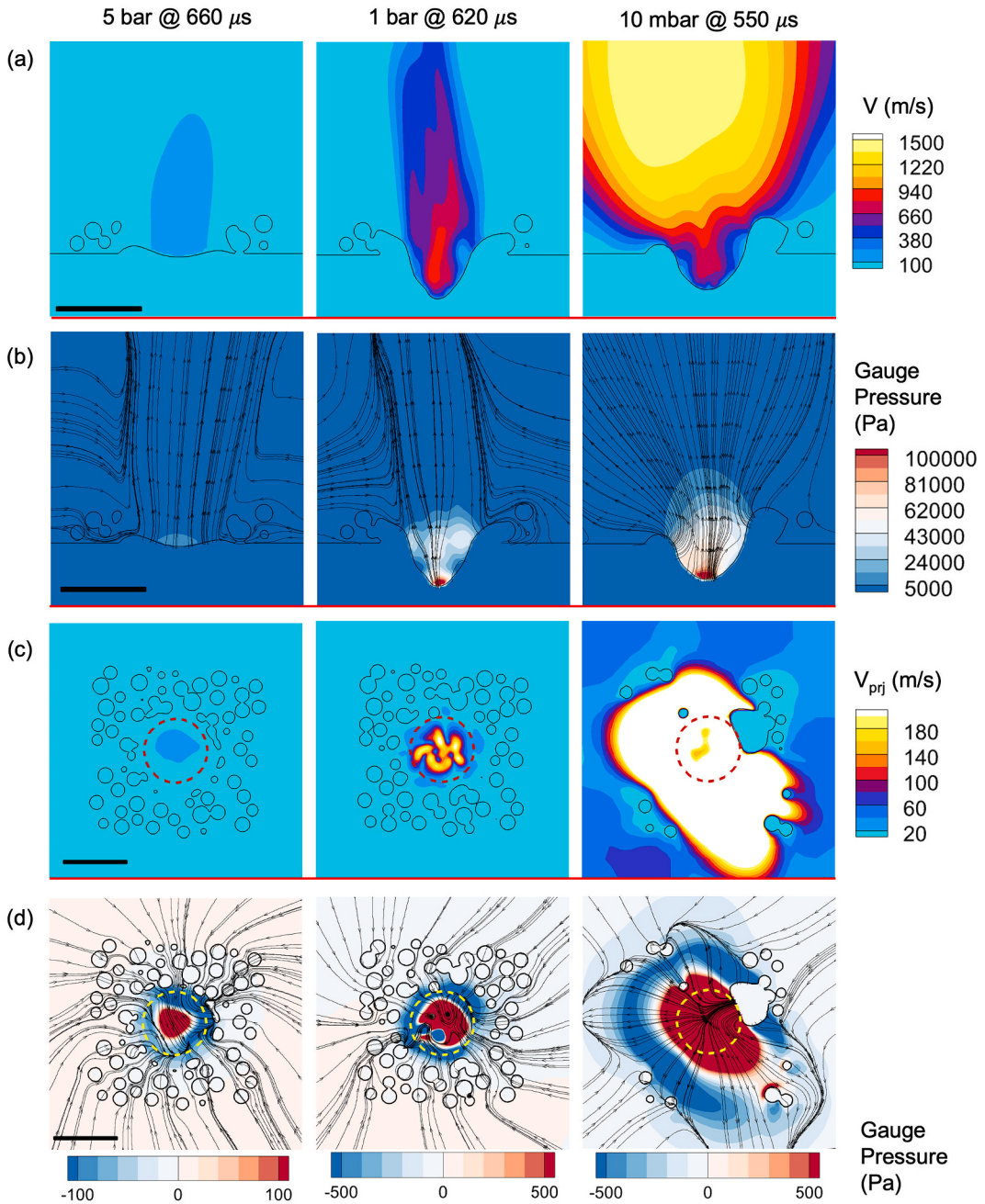


**Fig. 6.** Gas flow structure at the stable state is analyzed for  $p_{\text{amb}} = 5 \text{ bar}$ ,  $1 \text{ bar}$ , and  $10 \text{ mbar}$ . (a) Velocity magnitude at a vertical slice. The slicing location is the same as that shown in Fig. 2(c and d) and Fig. 5. (b) Gauge pressure and streamlines at the same vertical slice. (c) Projected (horizontal) velocity magnitude at a horizontal slice cutting through the powder bed. (d) Gauge pressure and streamlines at the same horizontal slice. The red and yellow dashed circle in (c, d) indicates the LIZ. All the scale bars are  $200 \mu\text{m}$ . (For interpretation of the references to colour in this figure legend, the reader is referred to the Web version of this article.)

assumption should be applied with caution.

It can be observed in Fig. 7(c) that the Knudsen number increases remarkably as the ambient pressure decreases. It is safe to assume that a continuum gas flow for high ambient pressure (5 bar), as  $Kn$  is 0.0004–0.004. The Knudsen number for the medium pressure (1 bar) is about 0.01, indicating the necessity of employing the slip boundary conditions even at the atmospheric pressure. The no-slip boundary condition should be carefully employed in gas flow simulations for LPBF, and it should be replaced by the slip boundary condition when  $Kn > 0.01$ . Under low ambient pressure (10 mbar),  $Kn$  is 0.05–0.5, which suggests that the continuum flow assumption will be invalid should the ambient pressure be further decreased. We stress that caution needs to be exercised when carrying out continuum fluid dynamics simulations

under extremely low ambient pressure levels for LPBF.

### 3.3. Powder motion driven by powder-gas interaction

The vapor jet and induced entrainment flow determine the powder-gas interaction, which drives the powder motion. The typical powder particle trajectories at 1 bar are shown in Fig. 8. An isometric view is given in Fig. 8(a), where five typical particle trajectories are shown in lines with circle markers (the triangle markers indicate the initial location). The red cylinder indicates the laser, and the box in light blue indicates the powder bed. The Y direction is the vertical direction, and (X, Z) are the two horizontal directions. Fig. 8(b–d) shows three projection views from the X-Z, X-Y, and Z-Y plane.

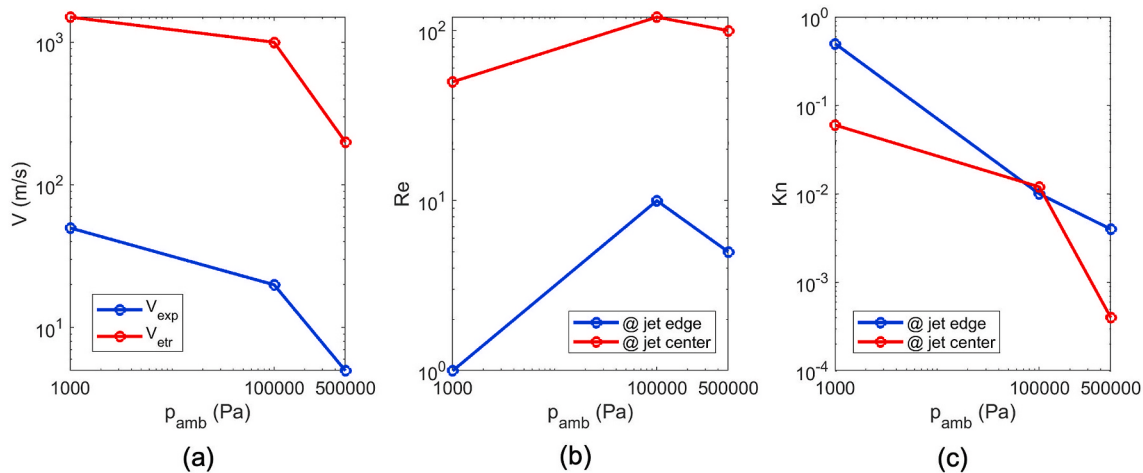


**Fig. 7.** Gas flow characteristics as a function of ambient pressure. (a) Characteristic vapor jet expansion velocity  $V_{exp}$  and induced entrainment velocity  $V_{etr}$ . (b) Reynolds number at the jet center and jet edge. (c) Knudsen number at the jet center and jet edge. All the quantities are extracted based on the vertical and horizontal slices shown in Fig. 6.

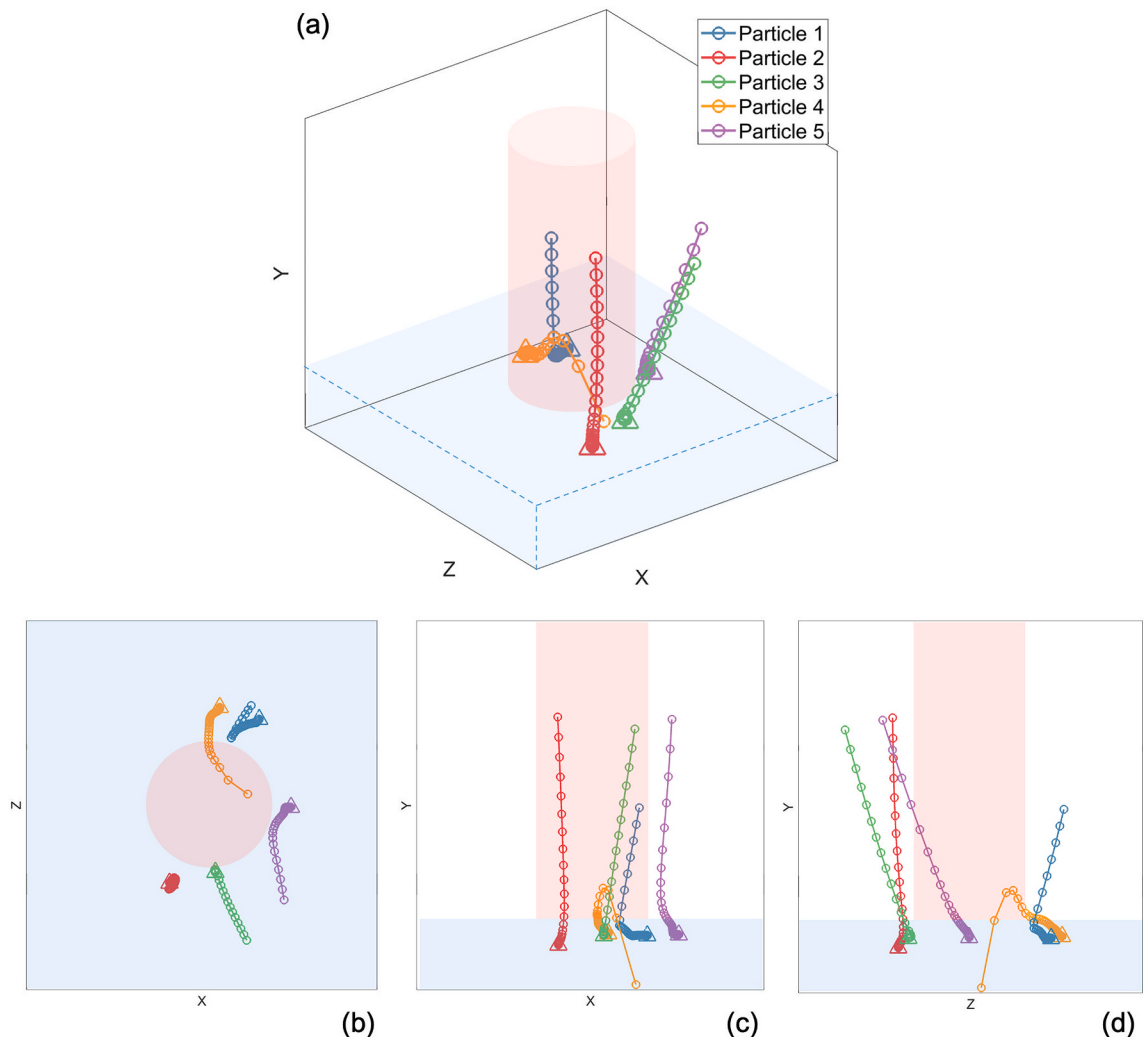


**Fig. 8.** Typical particle trajectories at 1 bar (atmospheric pressure). (a) Isometric view where the particle trajectories are lines with circle markers. The triangle marker indicates the initial locations of the particles. The red cylinder indicates the laser. The box in light blue indicates the powder bed. The Y direction is the horizontal direction, and (X, Z) are the two vertical directions. (b-d) Projected views of (a) from X-Z, X-Y, and Y-Z plane. (For interpretation of the references to colour in this figure legend, the reader is referred to the Web version of this article.)

These results confirmed the four characteristic models of powder-gas interaction that we identified with our previous 2D model. The four modes are briefly introduced below, with more details given in Ref. [29]:

- Recoil mode: It is defined when significant evaporation occurs on the surface of the powder particle, and the recoil pressure dominates over the drag force (gas-flow-induced force) on the particle surface. The powder particle is driven toward the opposite direction of the vapor jet by the recoil pressure.
- Entrainment mode: It is defined when the surroundings of the particle are dominated by the entrainment flow, and the particle is driven by the drag force towards the LIZ.
- Elevation mode: It is defined when the particle is simultaneously subject to the entrainment flow and the vapor jet expansion, and the particle is vertically ejected by the drag force with a relatively small divergence angle.
- Expulsion mode: It is defined when the surroundings of the particle are dominated by the expanding vapor jet, and the particle is ejected by the drag force with a relatively large divergence angle.

The powder motion can be governed by one powder-gas interaction mode or a sequence of modes. Specifically, for the simulation result in Fig. 8, Particles 1 and 5 are sequentially governed by the entrainment, elevation, and expulsion mode. They are entrained towards and subsequently ejected from the LIZ. Particle 2 is dominated by the elevation mode. It moves vertically upwards with neither entrainment nor ejection. Particle 3 is dominated by the expulsion mode. It is ejected by a tilted vapor jet with a large divergence angle. Particle 4 sequentially experiences the entrainment, elevation, and recoil mode. It is first entrained into the LIZ, and then evaporation occurs on its top surface due to laser heating. Finally, the recoil mode drives the particle to dive into the molten pool.

A new powder ejection mechanism, denoted as the “recoil-mode” powder ejection, is identified in the current simulations. Two typical powder particles governed by the recoil mode ejection are shown as Particles 6 and 7 in Fig. 9. Again, an isometric view is given in Fig. 9(a), and three projection views from the X-Z, X-Y, and Y-Z plane are given in Fig. 9(b-d). Particles 6 and 7 are first entrained and then ejected at a large ejecting angle (for Particle 7), or even downwards to the powder bed (for Particle 7). To quantify the transient situation for Particle 6, vertical planes can be determined by the laser centerline and the center

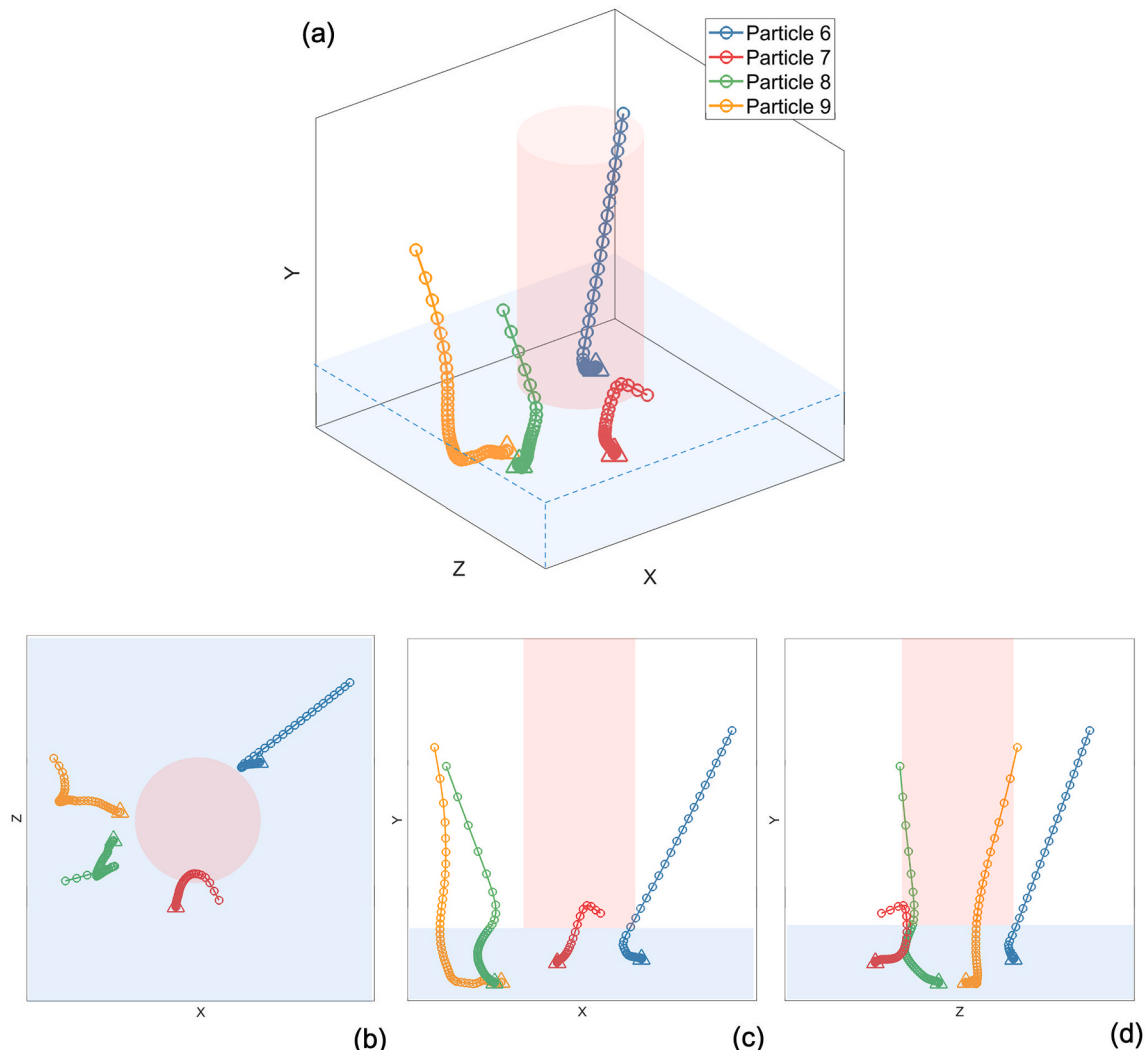


**Fig. 9. Miscellaneous powder particle trajectories.** Particle 6 is under  $p_{amb} = 3$  bar. Particle 7 is under  $p_{amb} = 5$  bar. Particles 8 and 9 are under  $p_{amb} = 50$  mbar. (a) Isometric view where the powder trajectories are lines with circle markers. The triangle marker indicates the initial locations of powder particles. The red cylinder indicates the laser. The box in light blue indicates the powder bed. The Y direction is the horizontal direction, and (X, Z) are the two vertical directions. (b-d) Projected views of (a) from X-Z, X-Y, and Y-Z plane. (For interpretation of the references to colour in this figure legend, the reader is referred to the Web version of this article.)

of Particle 6 at selected moments, and the temperature and flow field on the planes are shown in Fig. 10. The entrainment-ejection particle motion can be observed in Fig. 10(a) where Particle 6 is circled in red. Although the entrainment-ejection motion is similar to Particles 1 and 5 in Fig. 8, the driving force for the ejection is different. The temperature and flow field surrounding Particle 6 is zoomed in at two key moments ( $450 \mu\text{s}$  and  $530 \mu\text{s}$ ), as shown in Fig. 10(b and c). At  $450 \mu\text{s}$ , the upper left corner of Particle 6 cuts into the LIZ, and the laser heating causes significant local evaporation. As a result, the recoil pressure pushes the particle away from the LIZ and downwards to the powder bed. At  $530 \mu\text{s}$ , Particle 6 has departed from the LIZ but is heated at the lower left corner by the reflected laser beam. The reflected beam can be traced back to the asymmetric DZ clearly seen in Fig. 10(a). Therefore, Particle 6 is again subject to recoil pressure, and the latter subsequently ejects Particle 6 at a large ejecting angle. Particle 7 also cuts into the LIZ (Fig. 9(b)) when it is heated by the laser on its top (similar to the scenario in Fig. 10(b)). But Particle 7 is not subsequently heated by the reflected laser at its bottom position. Therefore, recoil pressure is only generated on the top of the particle to push it downwards to the powder bed. It is noted that the recoil-mode powder ejection is also inferred from experimental observations [1,5].

The recoil-mode powder ejection is found to be active only in the cases with medium- and high-pressure groups in Table 2. In the cases of medium pressure, the contribution of the recoil mode to the powder ejection is minor, and the powder ejection is primarily driven by the expulsion mode, where the expanding vapor jet exerts drag force on and ejects the powder particles. In the high-pressure conditions, the drag force becomes significantly smaller due to the reduced vapor jet velocity (Fig. 6). The expulsion mode weakens, and the recoil mode becomes the dominating mechanism for the powder ejection. As a result, the recoil-mode ejection is mostly distinguishable in the high-pressure simulations. As for the low-pressure cases, no recoil-mode ejection can be identified because the powder particles are typically ejected by the enhanced vapor jet expansion before they can be significantly heated by the laser.

Two new sequences of powder-gas interaction modes have also been identified that can cause complicated powder motions, as demonstrated by Particles 8 and 9 in Fig. 9. Fig. 9(c) shows a meandering trajectory for Particle 8: it is first ejected, then entrained, and finally ejected again. Particle 8 can be considered sequentially governed by the expulsion mode, entrainment mode, and again expulsion mode, which suggests a competition between the vapor jet expansion and the entrainment flow surrounding Particle 8. To visualize the competition, we extract the horizontal slices cutting through the center of Particle 8 at four moments, as shown in Fig. 11(a). As Particle 8 is elevating during this meandering motion, the slicing locations for the four moments in Fig. 11(a) are  $Y = 28.5 \mu\text{m}$ ,  $56.8 \mu\text{m}$ ,  $90.7 \mu\text{m}$ , and  $150.5 \mu\text{m}$ , respectively, with  $Y = 0$  being the substrate surface location. At  $230 \mu\text{s}$  in Fig. 11(a), Particle 8 (solid red circle) is ejected from the LIZ (dashed red circle) by the expanding vapor jet, governed by the expulsion mode. At  $420-580 \mu\text{s}$ , Particle 8 is away from the vapor jet expansion, and its surroundings are dominated by the entrainment flow, as shown by the zoomed-in flow field in Fig. 11(b and c). Therefore, Particle 8 is governed by the entrainment mode and is driven towards the LIZ. Finally, Particle 8 meets the expanding vapor jet again at  $680 \mu\text{s}$ ? Following this, Particle 8 is again governed by the expulsion mode and is ejected from the LIZ. It is noted that the ejection-entrainment motion of Particle 8 has also been observed in the experiments [12].

The second new sequence of powder-gas interaction modes manifests in Particle 9 (Fig. 9), which is sequentially governed by the ejection and elevation mode. There is a similar competition between the vapor jet expansion and the entrainment flow surrounding Particle 9. As can be seen in Fig. 9(c), Particle 9 is first ejected from the LIZ governed by the expulsion mode. As Particle 9 moves away from the LIZ, the vapor jet expansion weakens while the entrainment flow is strengthened. As the effects of these two flows are balanced, Particle 9 is governed by the elevation mode, which drives Particle 9 to move vertically upwards (Fig. 9(c and d)) with little horizontal movement (Fig. 9(b)).

As exemplified by Particles 8 and 9, the particles can be governed by new sequences of powder-gas interaction modes following their initial

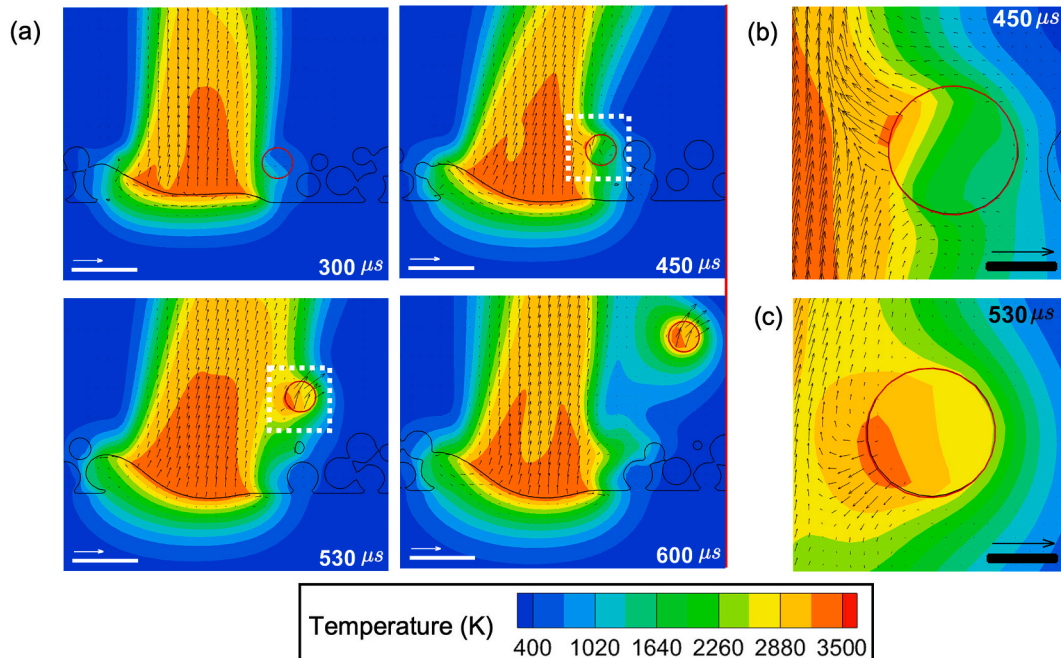


**Fig. 10.** Recoil-mode ejection under  $p_{\text{amb}} = 3 \text{ bar}$ . (a) Time sequence from a vertical slice formed by the laser centerline and the center of Particle 6 (red-circled). The slice shows the temperature and flow field. The scale bars are  $100 \mu\text{m}$ . The arrow keys are  $500 \text{ m/s}$  for the gaseous region and  $2 \text{ m/s}$  for the condensed region. (b, c) The temperature and flow field surrounding Particle 6 is zoomed in at  $450 \mu\text{s}$  and  $530 \mu\text{s}$ . The scale bars are  $25 \mu\text{m}$ . The arrow keys are  $250 \text{ m/s}$  for the gaseous region. The flow field inside the particle is not shown. (For interpretation of the references to colour in this figure legend, the reader is referred to the Web version of this article.)

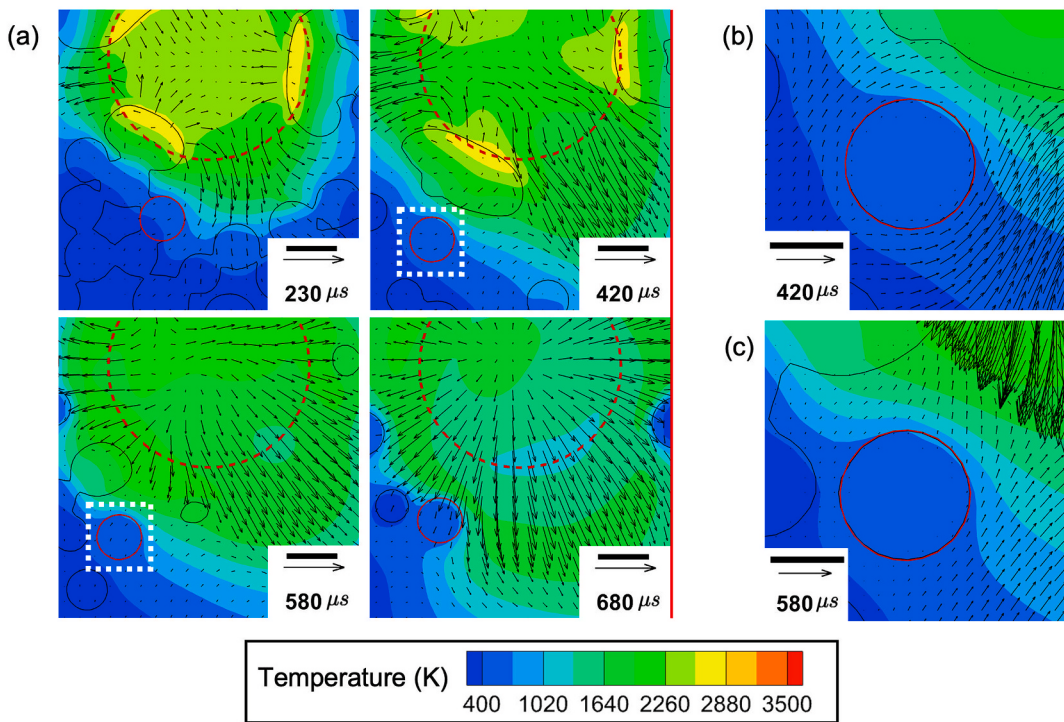


**Fig. 11. Meandering powder motion under  $p_{amb} = 5000$  mbar.** (a) Time sequence from a horizontal slice cutting through the center of Particle 8 (solid circle in red). The slices show the temperature and flow field. The red-dashed circle indicates the laser diameter (LIZ). The scale bars are 50  $\mu\text{m}$ . The arrow keys are 1000 m/s for the gaseous region and 4 m/s for the condensed region. (b, c) The temperature and flow field surrounding Particle 8 is zoomed in at 420  $\mu\text{s}$  and 580  $\mu\text{s}$ ? The scale bars are 25  $\mu\text{m}$ . The arrow keys are 50 m/s for the gaseous region. The flow field inside the particle is not shown. (For interpretation of the references to colour in this figure legend, the reader is referred to the Web version of this article.)

ejection from the LIZ, which leads to their complex motions. These new sequences of powder-gas interaction modes are caused by the balance (or imbalance) between the two driving forces stemming from the vapor jet expansion and the entrainment flow. It is noted that these sequences of modes and the consequent powder motions are almost exclusively observed in the low-pressure group (Table 2). This can be explained by the wide low-pressure ring observed under low ambient pressure (Fig. 6(d)), which creates more opportunities for the entrainment flow to balance or even overcome the vapor jet expansion, resulting in the new mode sequences and the complex powder motions. In contrast, the low-pressure ring observed for higher ambient pressure levels is narrow (Fig. 6(d)). Therefore, once the ejected powder particles pass the low-pressure ring, the weak entrainment flow is not adequate to alter the particle trajectory.

### 3.4. Statistical quantification of powder behavior

We have repeated the simulation four times at each ambient pressure level in Table 2 with random initial powder bed configurations. For each simulation, quantities such as velocity and average temperature can be tracked for each powder particle (examples are given in Appendix A). Statistical quantification is carried out to show the powder-related quantities as functions of ambient pressure, as shown in Fig. 12. The detailed definitions of the terms in Fig. 12 and the methods of extracting the values for these terms are given in Appendix B.

In Fig. 12(a), the magnitudes of the drag and recoil forces (defined in Appendix B) on powder particles are shown as functions of the ambient pressure. The drag forces (both for powder entrainment and ejection) are the maximum at the medium-pressure levels. In the cases of the high-pressure levels, the drag forces are reduced because the gas flow velocity (both vapor jet expansion and induced entrainment flow) is small, as shown in Fig. 6(a, c). In the cases of the low-pressure levels, although the gas flow velocity is increased, the flow enters the “slip flow” regime, and

the drag force decreases with the increasing Knudsen number [33]. The ejection drag force ( $10^{-6} - 10^{-5}$  N) is typically one magnitude larger than the entrainment drag force ( $10^{-7} - 10^{-6}$  N) for all ambient pressure levels. The recoil force, in most cases, only briefly occurs on the top surface of powder particles when the vapor jet begins to form. The particles subject to the recoil force then rapidly merge into the molten pool. In this scenario, the magnitude of recoil force ( $10^{-5}$  N) does not significantly change with the ambient pressure. At medium and high ambient pressure levels, however, a few particles can have a larger recoil force (up to  $\sim 10^{-4}$  N) when they are ejected (e.g., Particles 6 and 7 in Fig. 9) or dives into the molten pool (e.g., Particle 2 in Fig. 8) driven by the recoil mode. This explains the larger error bar for medium and high ambient pressure levels in Fig. 12(a).

Next, the occurrences of entrained and ejected particles (defined in Appendix B) are counted in Fig. 12(b) as functions of the ambient pressure. It is observed that the occurrence of ejected particles increases with decreasing ambient pressure, which is due to the enhanced vapor jet expansion. The occurrence of entrained particles first increases with decreasing ambient pressure but decreases at the lowest pressure level (10 mbar, i.e.,  $10^3$  Pa). The increase of entrained particles can be attributed to the wider low-pressure ring under lower ambient pressure (Fig. 6(d)). However, the entrainment drag is reduced significantly at the lowest pressure level, as discussed in Fig. 12(a), which explains the decrease of entrained particles.

The entrainment and ejection particle velocity (defined in Appendix B) are plotted as functions of the ambient pressure in Fig. 12(c). The particle velocities are the maximum at the medium pressure levels and decrease for lower or higher pressure levels, which is consistent with the trend for the entrainment and ejection drags in Fig. 12(a). For high ambient pressure levels, the ejection velocity is typically smaller due to the smaller ejection drag. However, when the recoil-mode ejection occurs, the ejection velocity can be large despite the smaller drag force. Therefore, there is an increase in ejection velocity for the highest

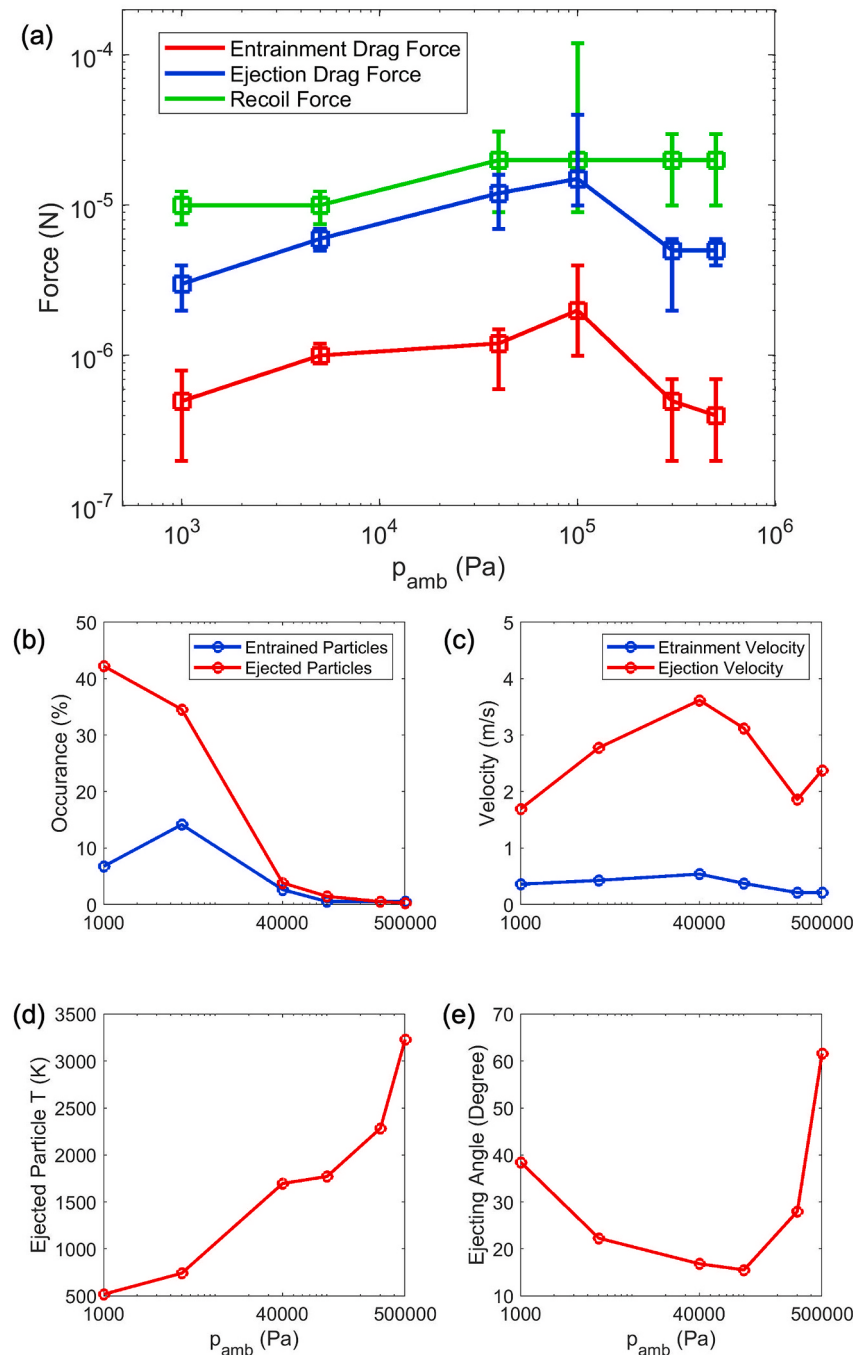


**Fig. 12. Statistical quantification of powder behavior as a function of the ambient pressure.** The definitions of the terms in (a–e) and the method of extracting these pieces of information are detailed in Appendix B. (a) Magnitudes of the entrainment drag, ejection drag, and recoil forces. (b) Occurrences of the entrained and ejected particles. (c) Entrainment and ejection velocities. (d) The temperature of the ejected particles. (e) The ejecting angle of the ejected particles.

pressure level (5 bar, or  $5 \times 10^5$  Pa).

It is noticed in Fig. 12(c) that the entrainment velocity ( $\sim 0.5$  m/s) is typically smaller than the ejection velocity ( $\sim 3$  m/s). The velocity magnitude can only be qualitatively compared with X-ray imaging results, as the particle velocity observed in X-ray imaging is only the projected velocity. Typical particle trajectories are manually extracted from the X-ray imaging to calculate the projected particle velocity (examples given in Appendix A). The measured maximum velocity in a particle's lifespan agrees with the range 0.5–3 m/s in Fig. 12(c).

Finally, the temperature and ejecting angle (defined in Appendix B) of the ejected particles are quantified as functions of the ambient pressure, as shown in Fig. 12(d and e). As can be seen in Fig. 12(d), the

temperature of the ejected particles increases from 500 K to almost 3500 K as the ambient pressure increases from 10 mbar ( $1 \times 10^3$  Pa) to 5 bar ( $5 \times 10^5$  Pa). This trend agrees with the observation in Ref. [14] and can be explained as follows. Under high ambient pressure, the boiling temperature of the metal is increased, and therefore, the powder particles can be further heated before being ejected by the vapor jet.

In Fig. 12(e), it is observed that the ejecting angle is increased from  $\sim 15^\circ$  to  $\sim 40^\circ$  as the ambient pressure decreases from 1 bar ( $1 \times 10^5$  Pa) to 10 mbar ( $1 \times 10^3$  Pa). This is because the vapor jet expansion is subject to less confinement at lower pressure levels (Fig. 5(c)). As a result, the vapor jet expands at a larger diverging angle and causes a larger ejecting angle for the ejected particles. This trend also agrees with

the findings in Ref. [12]. As the ambient pressure increases from 1 bar ( $1 \times 10^5$  Pa) to 5 bar ( $5 \times 10^5$  Pa), the ejecting angle dramatically increases due to the increasingly frequent occurrence of recoil-mode ejection. The recoil-mode ejection can cause a large ejecting angle, even larger than  $90^\circ$ , when the particle is ejected downwards to the powder bed (e.g., Particle 7 in Fig. 9).

#### 4. Discussion on powder motion mitigation

The simulation results show that a high ambient pressure can significantly suppress the gas flow (Fig. 6), and therefore, reduce the drag forces (Fig. 12(a)) and the occurrences of powder entrainment and ejection (Fig. 12(b)). This suggests that applying of a high ambient pressure can be an effective way to mitigate powder motion. The effects of hyper-atmospheric conditions (3 bar and 5 bar) have been experimentally investigated in Ref. [14] with a moving laser. The authors found that the number of entrained particles decreases with the ambient pressure, which agrees with the current simulation results. However, the authors also found that the number of ejected particles increases with the ambient pressure, which is different from the current simulation results for a stationary laser. This discrepancy can be explained as follows. In a stationary-laser process under high ambient pressure, the particles illuminated by the laser beam center are melted and merged into the molten pool, and the particles outside the laser illumination will not have significant motion because the gas flow is suppressed under high ambient pressure. Only the particles illuminated by the rim of the laser can potentially be ejected by the recoil-mode ejection (Fig. 10). As the number of particles in the rim of the laser is low for a stationary laser, few particle ejection events are possible. And if those particles are successfully ejected, no more particles will be entrained to the rim of the laser and then be ejected, so the powder ejection will not continue. The situation is very different with a moving laser. As the laser moves along a given contour, it constantly catches new particles in its moving rim. All the particles on the laser scanning contour will be caught by the rim of the laser at certain moments and likely be ejected by the recoil-mode ejection. Therefore, the high ambient pressure may not reduce the powder ejection in a moving-laser case, and under the conditions in Ref. [14], the high ambient pressure even increases the powder ejection. Moreover, the ejected particles under high ambient pressure are typically in a molten state (Fig. 12(d)) and have a large divergence angle (Fig. 12(e)). They can stick with other particles to form agglomerates, which can grow through a “snow-balling” mechanism [5], that the agglomerates can be later ejected again and stick with more particles. This is confirmed in Ref. [14], where the authors found more powder spatter with larger size and temperature under high ambient pressure conditions.

Based on the above reasoning, we propose a new strategy that can potentially mitigate the powder motion in a moving-laser process: applying a high ambient pressure along with a pulsed laser beam. The pulsed laser beam moves in consecutive points and remains at each point for a certain amount of time (exposure time) before moving to the next point. We expect two beneficial effects from this strategy: (1) only the particles illuminated by the rim of the laser beam of each pulse can be ejected by the recoil-mode ejection. Therefore, the number of potential ejected particles is reduced compared to the continuous moving laser. (2) the point distance between two consecutive points and the exposure time can be optimized to further reduce powder ejection. For example, the point distance and exposure time can be adjusted so that the particles at the rim of the previous pulse will fall in the center of the next pulse before they can be ejected.

It is noted that the use of pulsed laser beam in LPBF has been reported in the literature [40–43], but the laser pulsating is used to control the molten pool stability, the cooling rate, and the microstructure. To the best of our knowledge, the effects of pulsed laser on the powder motion have not been investigated. It is also emphasized that a pulsed laser can only effectively mitigate powder motion in a high ambient

pressure. Under medium and low ambient pressure levels, surrounding particles will continuously move toward the rim of the laser through the entrainment mode and then be ejected through the elevation or expulsion modes. In the future, we will perform X-ray imaging experiments and numerical simulations to examine the effectiveness of this proposed strategy.

#### 5. Conclusion

In this work, a 3D multiphysics model is developed that fully couples the molten pool dynamics, gas flow, and powder motion in LPBF. The model capabilities highlight in resolving the gas flow surrounding the powder particles, as well as quantifying the forces exerted on the particle surfaces. In a “spot-welding” setup, simulations are carried out to investigate the effects of the ambient pressure (in the range of 10 mbar–5 bar) on the gas flow, powder-gas interaction, and powder behavior. The temperature, flow velocity, and pressure field in the gas under different ambient pressure levels are first quantified. Then, characteristic powder motions are examined and explained by the powder-gas interaction mode(s). Finally, the powder behavior (e.g., velocity, temperature, and ejecting angle) is statistically analyzed as a function of the ambient pressure. The model predictions of powder motion agree well with the high-speed X-ray imaging experiments.

A consistent gas flow pattern is observed in simulations for all ambient pressure levels investigated. The vapor jet initiates from the DZ and expands into the ambient, while the ambient gas is entrained towards the LIZ. The vapor jet expansion is driven by a pressure decrease from the DZ bottom towards the DZ opening. The entrainment flow is driven by a pressure decrease from the ambient towards the LIZ. As the ambient pressure decreases from 5 bar to 10 mbar, the major effects on the gas flow are summarized as follows:

- The characteristic velocity of vapor jet expansion increases from 200 m/s to 1500 m/s. The characteristic velocity of the entrainment flow increases from 5 m/s to 50 m/s.
- The divergent angle of the vapor jet expansion significantly increases.
- The characteristic temperature of the vapor jet decreases from 3400 K to 2100 K.
- The Knudsen number of the gas flow increases from the range (0.004–0.004) to the range (0.05–0.5). The gas flow enters the slip flow regime ( $Kn > 0.01$ ) when the ambient pressure is about 1 bar. It is expected that the continuum assumption of the gas flow fails ( $Kn \gtrsim 0.2$ ) when the ambient pressure is below 10 mbar.

The four powder-gas interaction modes previously identified in the 2D simulations (i.e., recoil, entrainment, elevation, and expulsion modes) are confirmed in the current 3D simulations. The motion of a specific powder particle can be attributed to that the particle being subject to a single powder-gas interaction mode or a sequence of modes. More knowledge regarding the interaction modes and the resultant powder motion have been revealed with the 3D simulation results. Specifically, the recoil mode is found as another cause for the powder ejection besides the expulsion mode. Such recoil-mode ejection is mostly distinguished at ambient pressure levels above 1 bar. New sequences of powder-gas interaction modes are also found at ambient pressure levels below 400 mbar. The expulsion-elevation mode sequence causes the powder particle to elevate after being ejected from the LIZ. The expulsion-entrainment-expulsion mode sequence causes the particle to have a meandering motion.

From a statistical analysis, the major effects of the ambient pressure on the powder-related quantities are summarized as follows:

- The number of ejected particles monotonically increases as the ambient pressure is decreased.

- The ejection drag force on the particle has a magnitude of  $10^{-6}$  –  $10^{-5}$  N. It is the maximum when the ambient pressure is at a medium level ( $\sim 1$  bar). The entrainment drag force has a magnitude of  $10^{-7}$  –  $10^{-6}$  N and also peaks at  $\sim 1$  bar. The recoil force has a magnitude of  $\sim 10^{-5}$  N and does not significantly change with the ambient pressure.
- The ejection velocity of the particle is about 2–4 m/s. The entrainment velocity is about 0.5 m/s. For both velocities, the maximum velocity is achieved at  $\sim 400$  mbar.
- The temperature of the ejected particles monotonically increases from  $\sim 500$  K to  $\sim 3500$  K, as the ambient pressure is increased from 10 mbar to 5 bar.

The current 3D model provides quantitative information regarding the gas flow, powder-gas interaction, and powder behavior. Based on the above information, we propose that implementing a pulsed laser under a high ambient pressure can reduce the powder motion in LPBF.

#### Author contribution

Xuxiao Li - software, investigation, writing – original draft. Qilin Guo - investigation, writing – review & editing. Lianyi Chen - conceptualization, funding acquisition, project administration. Wenda

Tan - conceptualization, funding acquisition, project administration, writing – review & editing.

#### Declaration of competing interest

The authors declare that they have no known competing financial interests or personal relationships that could have appeared to influence the work reported in this paper.

#### Acknowledgements

X.L and W.T acknowledge the financial support provided by the National Science Foundation under Grant No. CMMI-1933368 and the technical support from the Center for High-Performance Computing at the University of Utah. Q.G and L.C acknowledge the financial support by the National Science Foundation under Grant No. CMMI-2002840. This research used resources of the Advanced Photon Source, a U.S. Department of Energy (DOE) Office of Science User Facility, operated for the DOE Office of Science by Argonne National Laboratory under Contract No. DE-AC02-06CH11357. The authors also thank Dr. Kamel Fezzaa and Dr. Tao Sun at the APS for their help on the beamline experiments and the fruitful discussions.

#### Appendix A. Tracking powder-related quantities for simulations and experiments

For each powder particle in the simulation, the angular velocity, torque, velocity, forces ( $F_p$  and  $F_v$ ), and average temperature can be tracked with respect to time. The tracking of Particles 1–5 in Fig. 8 is given in Fig. A1, and the tracking of Particles 6–9 in Fig. 9 is given in Fig. A2, as examples.  $F_p$  is the force (magnitude) integrated by the pressure distribution (including recoil pressure if evaporation occurs) on the particle surface.  $F_v$  is the force (magnitude) integrated by the viscous stress distribution on the particle surface. These integrations are performed numerically using the “Lagrangian points” [29] on the particle surface. The average temperature of the particle is calculated by averaging the temperature of the cells inside a particle from the CFD computation. The particle tracking is terminated once the particle moves out of the calculation domain or merges into the molten pool.

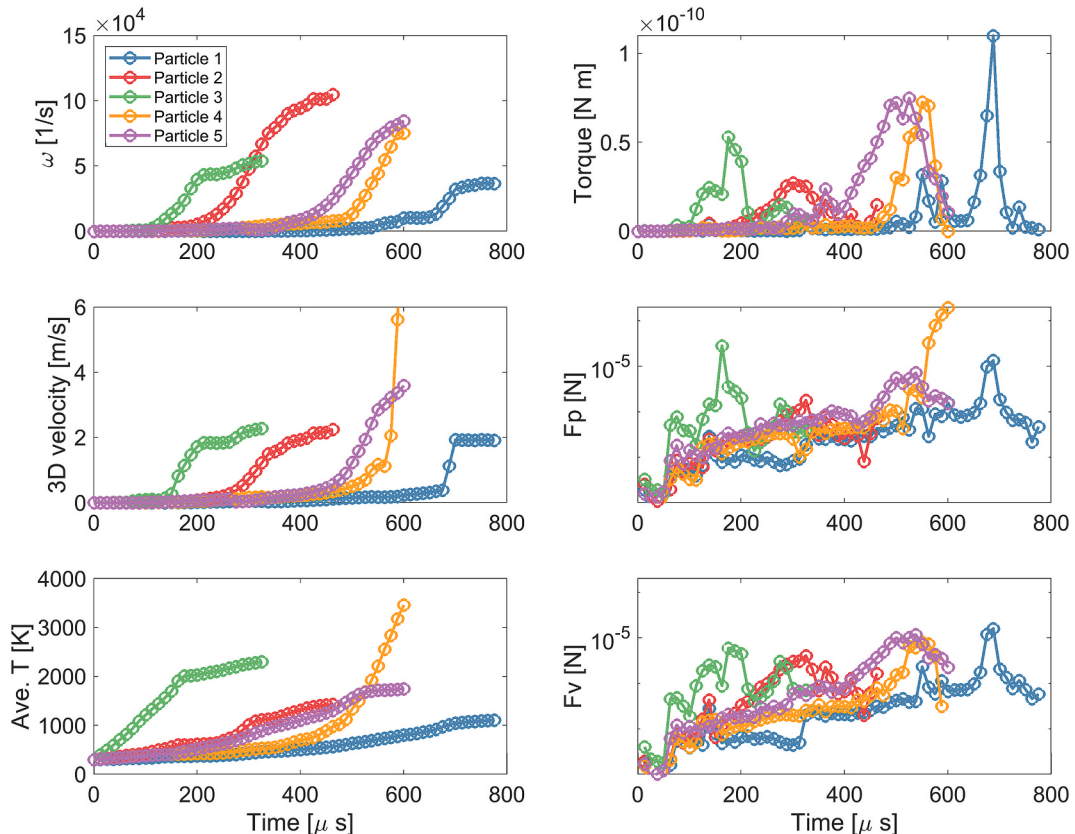


Fig. A1. Tracking of the angular velocity, torque, velocity, forces, and average temperature of Particles 1–5 (in Fig. 8) with respect to time.

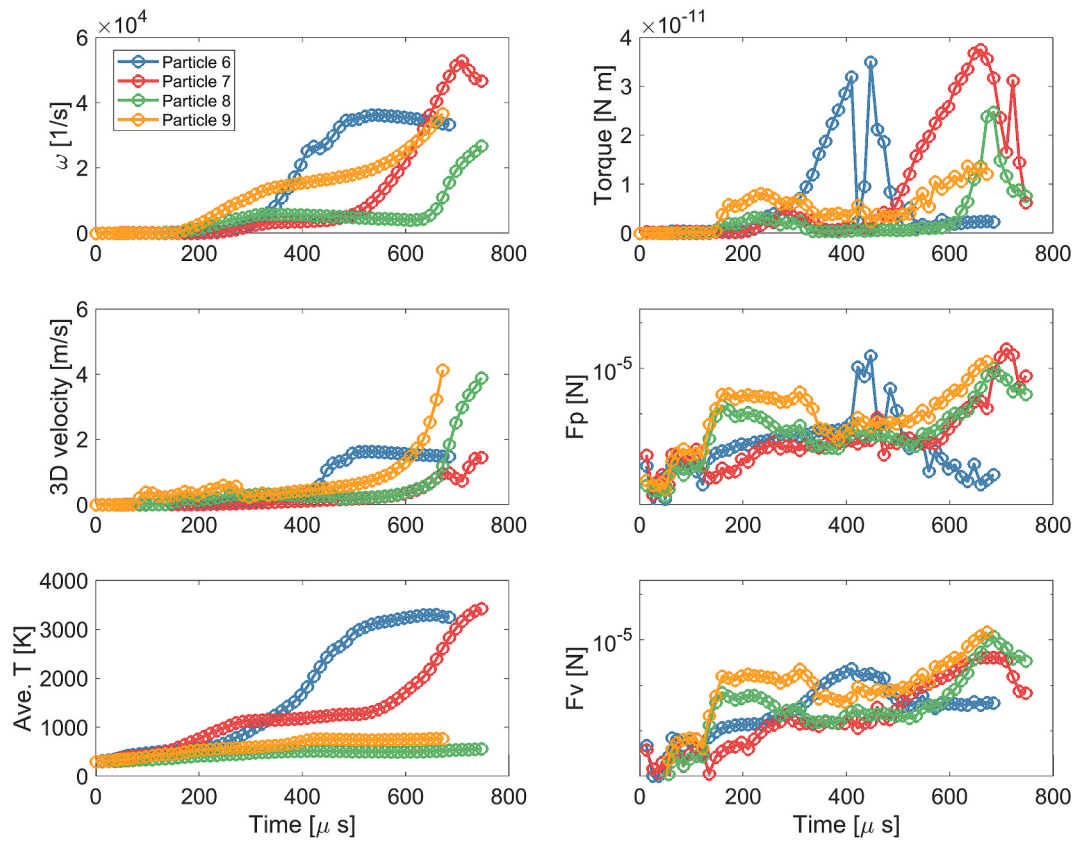


Fig. A2. Tracking of the angular velocity, torque, velocity, forces, and average temperature of Particles 6–9 in (Fig. 9) with respect to time.

The projected particle trajectories are manually extracted from the high-speed X-ray imaging, and the projected particle velocities can be calculated from the particle trajectories. Examples are shown in Fig. A3. The maximum projected velocities in a particle's lifespan are comparable to the velocity magnitude (0.5–3 m/s) shown in Fig. 12(c).

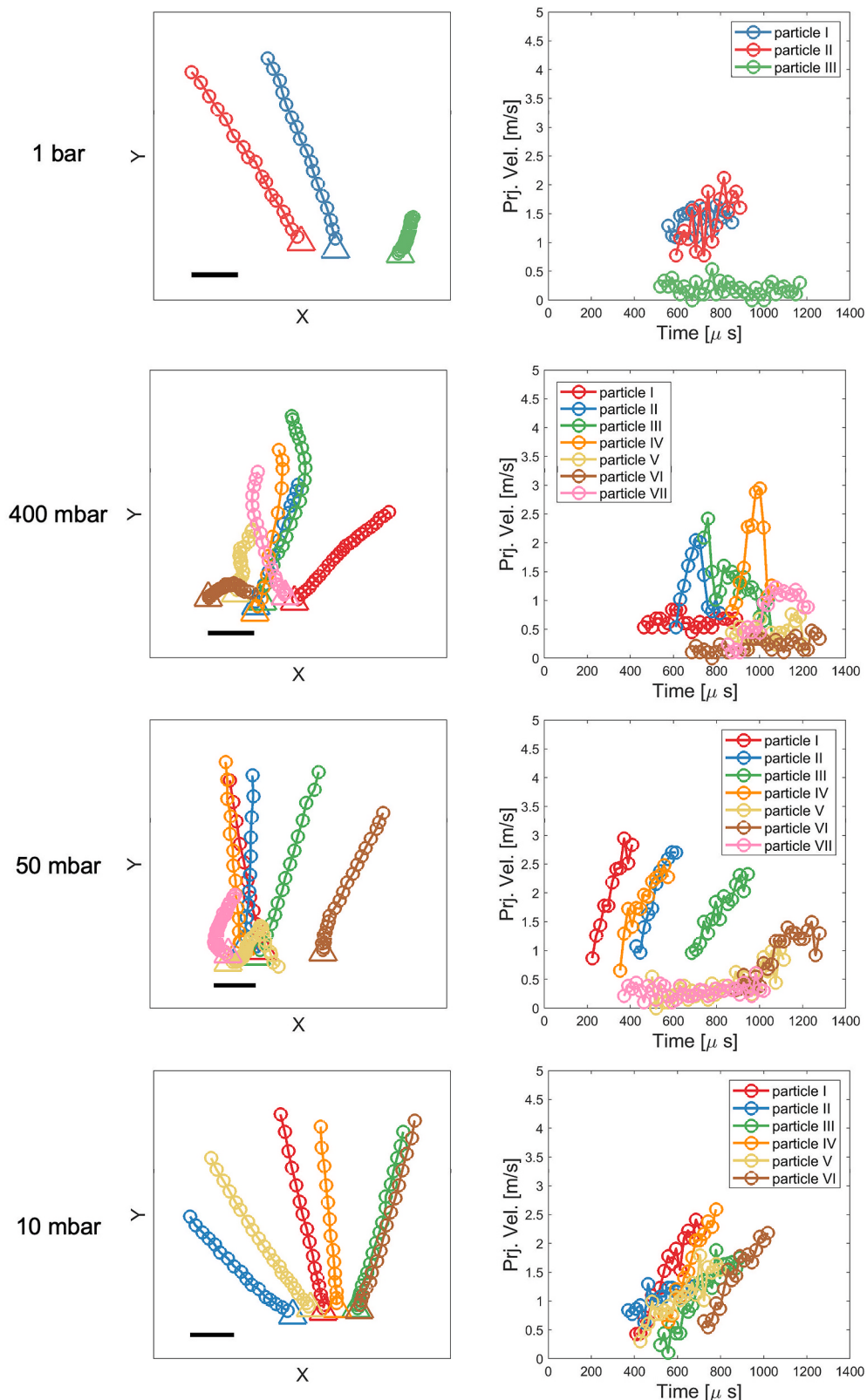


Fig. A3. Typical projected particle trajectories and velocities manually tracked from high-speed X-ray imaging results. All scale bars are 100  $\mu\text{m}$ .

#### Appendix B. Details on statistical quantification of powder behavior

For each simulation, The “entrained particle” and the “ejected particle” are defined as follows. If a powder particle moves towards the LIZ from the X-Z projection view, e.g., Fig. 8(b) and Fig. 9(b), for a projected distance larger than 50  $\mu\text{m}$ , it is defined as an entrained particle. If a particle moves

away from the LIZ for a distance larger than 50  $\mu\text{m}$  (not projected distance), it is defined as an ejected particle. It is noted a particle can be both an entrained particle and an ejected particle.

For each entrained particle, the projected (X-Z plane) drag force on the particle when it is entrained (i.e., moving towards the LIZ) is defined as the “entrainment drag.” For each ejected particle, the drag force (not projected) on the particle when it is ejected (i.e., moving away from the LIZ) is defined as the “ejection drag.” For both the entrained and ejected particle, the recoil force is defined as the force (not projected) exerted on the particle by the recoil pressure if there is any evaporation occurs on the particle surface. Based on these definitions, we can identify the maximum entrainment drag, ejection drag, and recoil force for each entrained/ejected particle during its lifespan. Finally, we average these maximum forces over all entrained/ejected particles in the simulations and plot the averaged value in Fig. 12(a). The range of these maximum forces is indicated by the error bars in Fig. 12(a). The occurrences of the entrained and ejected particles are normalized by the total amount of particles in the powder bed, as shown in Fig. 12(b).

In Fig. 12(c), the entrainment and ejection velocities are defined as follows. For each entrained particle, the projected (X-Z plane) velocity when the particle is entrained is defined as the “entrainment velocity.” For each ejected particle, the velocity (not projected) when the particle is ejected is defined as the “ejection velocity.” Based on these definitions, we can identify the maximum entrainment and ejection velocity for each entrained/ejected particle during its lifespan. Finally, we average these maximum velocities over all entrained/ejected particles in the simulations and plot the averaged values in Fig. 12(c).

For each ejected particle, we can identify the maximum particle (average) temperature when it is ejected. We average the maximum particle temperature over all ejected particles and plot the averaged values in Fig. 12(d). Also, for each ejected particle, the last simulated moment when the particle is ejected is used to calculate the ejecting angle. The ejecting angle is calculated by  $\arccos(v_y/v)$ , where  $v$  is the particle velocity magnitude and  $v_y$  is the vertical component of velocity. We average the ejecting angle over all the ejected particles and plot the averaged values in Fig. 12(e).

## Appendix C. Supplementary data

Supplementary data related to this article can be found at <https://doi.org/10.1016/j.ijmachtools.2021.103797>.

## References

- [1] S. Ly, A.M. Rubenchik, S.A. Khairallah, G. Guss, M.J. Matthews, Metal vapor micro-jet controls material redistribution in laser powder bed fusion additive manufacturing, *Sci. Rep.* 7 (1) (2017) 4085.
- [2] P. Bidare, I. Bitharas, R. Ward, M. Attallah, A. Moore, Fluid and particle dynamics in laser powder bed fusion, *Acta Mater.* 142 (2018) 107–120.
- [3] C. Zhao, K. Fezzaa, R.W. Cunningham, H. Wen, F. De Carlo, A.D. Rollett, T. Sun, Real-time monitoring of laser powder bed fusion process using high-speed X-ray imaging and diffraction, *Sci. Rep.* 7 (1) (2017) 3602.
- [4] M.J. Matthews, G. Guss, S.A. Khairallah, A.M. Rubenchik, P.J. Depond, W.E. King, Denudation of metal powder layers in laser powder bed fusion processes, *Acta Mater.* 114 (2016) 33–42.
- [5] Z.A. Young, Q. Guo, N.D. Parab, C. Zhao, M. Qu, L.I. Escano, K. Fezzaa, W. Everhart, T. Sun, L. Chen, Types of spatter and their features and formation mechanisms in laser powder bed fusion additive manufacturing process, *Addit. Manuf.* 36 (2020) 101438.
- [6] U. Ali, R. Esmaeilzadeh, F. Ahmed, D. Sarker, W. Muhammad, A. Keshavarzkermani, Y. Mahmoodkhani, E. Marzbanrad, E. Toyserkani, Identification and characterization of spatter particles and their effect on surface roughness, density and mechanical response of 17-4 PH stainless steel laser powder-bed fusion parts, *Mater. Sci. Eng., A* 756 (2019) 98–107.
- [7] S.A. Khairallah, et al., Controlling interdependent meso-nanosecond dynamics and defect generation in metal 3D printing, *Science* 368 (6491) (2020) 660–665.
- [8] M. Simonelli, et al., A study on the laser spatter and the oxidation reactions during selective laser melting of 316L stainless steel, Al-Si10-Mg, and Ti-6Al-4V, *Mater. Trans. 46* (9) (2015) 3842–3851.
- [9] A.T. Polonsky, T.M. Pollock, Closing the science gap in 3D metal printing, *Science* 368 (6491) (2020) 583–584.
- [10] D. Wang, G. Ye, W. Dou, M. Zhang, Y. Yang, S. Mai, Y. Liu, Influence of spatter particles contamination on densification behavior and tensile properties of CoCrW manufactured by selective laser melting, *Opt. Laser. Technol.* 121 (2020) 105678.
- [11] L.E. Criales, Y.M. Arisoy, B. Lane, S. Moylan, A. Donmez, T. Özal, Laser powder bed fusion of nickel alloy 625: experimental investigations of effects of process parameters on melt pool size and shape with spatter analysis, *Int. J. Mach. Tool Manufact.* 121 (2017) 22–36.
- [12] Q. Guo, C. Zhao, L.I. Escano, Z. Young, L. Xiong, K. Fezzaa, W. Everhart, B. Brown, T. Sun, L. Chen, Transient dynamics of powder spattering in laser powder bed fusion additive manufacturing process revealed by in-situ high-speed high-energy x-ray imaging, *Acta Mater.* 151 (2018) 169–180.
- [13] P. Bidare, I. Bitharas, R.M. Ward, M.M. Attallah, A.J. Moore, Laser powder bed fusion at sub-atmospheric pressures, *Int. J. Mach. Tool Manufact.* 130 (2018) 65–72.
- [14] P. Bidare, I. Bitharas, R.M. Ward, M.M. Attallah, A.J. Moore, Laser powder bed fusion in high-pressure atmospheres, *Int. J. Adv. Manuf. Technol.* 99 (1–4) (2018) 543–555.
- [15] S. Traore, M. Schneider, I. Koutiri, F. Coste, R. Fabbro, C. Charpentier, P. Lefebvre, P. Peyre, Influence of gas atmosphere (Ar or He) on the laser powder bed fusion of a Ni-based alloy, *J. Mater. Process. Technol.* 288 (2020) 116851.
- [16] C. Pauzon, P. Forêt, E. Hryha, T. Arunprasad, L. Nyborg, Argon-helium mixtures as Laser-Powder Bed Fusion atmospheres: towards increased build rate of Ti-6Al-4V, *J. Mater. Process. Technol.* 279 (2020) 116555.
- [17] I. Bitharas, A. Burton, A.J. Ross, A.J. Moore, Visualisation and numerical analysis of laser powder bed fusion under cross-flow, *Additive Manufacturing* (2020) 101690.
- [18] L. Kaserer, S. Bergmueller, J. Braun, G. Leichtfried, Vacuum laser powder bed fusion—track consolidation, powder denudation, and future potential, *Int. J. Adv. Manuf. Technol.* 110 (11) (2020) 3339–3346.
- [19] C. Tang, K.Q. Le, C.H. Wong, Physics of humping formation in laser powder bed fusion, *Int. J. Heat Mass Tran.* 149 (2020) 119172.
- [20] S. Shrestha, K. Chou, A build surface study of Powder-Bed Electron Beam Additive Manufacturing by 3D thermo-fluid simulation and white-light interferometry, *Int. J. Mach. Tool Manufact.* 121 (2017) 37–49.
- [21] M. Bayat, A. Thanki, S. Mohanty, A. Witvrouw, S. Yang, J. Thorborg, N.S. Tiedje, J. H. Hattel, Keyhole-induced porosities in laser-based powder bed fusion (L-PBF) of Ti6Al4V: high-fidelity modelling and experimental validation, *Addit. Manuf.* 30 (2019) 100835.
- [22] M. Xia, D. Gu, G. Yu, D. Dai, H. Chen, Q. Shi, Porosity evolution and its thermodynamic mechanism of randomly packed powder-bed during selective laser melting of Inconel 718 alloy, *Int. J. Mach. Tool Manufact.* 116 (2017) 96–106.
- [23] S.A. Khairallah, A.T. Anderson, A. Rubenchik, W.E. King, Laser powder-bed fusion additive manufacturing: physics of complex melt flow and formation mechanisms of pores, spatter, and denudation zones, *Acta Mater.* 108 (2016) 36–45.
- [24] D. Gu, M. Xia, D. Dai, On the role of powder flow behavior in fluid thermodynamics and laser processability of Ni-based composites by selective laser melting, *Int. J. Mach. Tool Manufact.* 137 (2019) 67–78.
- [25] W. Yan, W. Ge, Y. Qian, S. Lin, B. Zhou, W.K. Liu, F. Lin, G.J. Wagner, Multi-physics modeling of single/multiple-track defect mechanisms in electron beam selective melting, *Acta Mater.* 134 (2017) 324–333.
- [26] A. Bauereiß, T. Scharowsky, C. Körner, Defect generation and propagation mechanism during additive manufacturing by selective beam melting, *J. Mater. Process. Technol.* 214 (11) (2014) 2522–2528.
- [27] Y.A. Mayi, M. Dal, P. Peyre, M. Bellet, C. Metton, C. Moriconi, R. Fabbro, Laser-induced plume investigated by finite element modelling and scaling of particle entrainment in laser powder bed fusion, *J. Phys. Appl. Phys.* 53 (7) (2019), 075306.
- [28] H. Chen, W. Yan, Spattering and denudation in laser powder bed fusion process: multiphase flow modelling, *Acta Mater.* 196 (2020) 154–167.
- [29] X. Li, C. Zhao, T. Sun, W. Tan, Revealing transient powder-gas interaction in laser powder bed fusion process through multi-physics modeling and high-speed synchrotron x-ray imaging, *Addit. Manuf.* 35 (2020) 101362.
- [30] N. Kouraytem, X. Li, R. Cunningham, C. Zhao, N. Parab, T. Sun, A.D. Rollett, A. D. Spear, W. Tan, Effect of laser-matter interaction on molten pool flow and keyhole dynamics, *Phys. Rev. Appl.* 11 (6) (2019), 064054.
- [31] W. Tan, N.S. Bailey, Y.C. Shin, Investigation of keyhole plume and molten pool based on a three-dimensional dynamic model with sharp interface formulation, *J. Phys. Appl. Phys.* 46 (5) (2013), 055501.
- [32] W. Tan, Y.C. Shin, Analysis of multi-phase interaction and its effects on keyhole dynamics with a multi-physics numerical model, *J. Phys. Appl. Phys.* 47 (34) (2014) 345501.
- [33] R.L. Panton, *Incompressible Flow*, John Wiley & Sons, 2013.
- [34] G.A. Bird, J.M. Brady, *Molecular Gas Dynamics and the Direct Simulation of Gas Flows*, Clarendon press Oxford, 1994.
- [35] W.S. Jodrey, E.M. Tory, Simulation of random packing of spheres, *Simulation* 32 (1) (1979) 1–12.

- [36] K.C. Mills, Recommended Values of Thermophysical Properties for Selected Commercial Alloys, Woodhead Publishing, 2002.
- [37] C.S. Kim, Thermophysical properties of stainless steels, Argonne National Lab., Ill. (USA), 1975.
- [38] P. Pichler, B.J. Simonds, J.W. Sowards, G. Pottlacher, Measurements of thermophysical properties of solid and liquid NIST SRM 316L stainless steel, *J. Mater. Sci.* 55 (9) (2020) 4081–4093.
- [39] A.B. Murphy, The effects of metal vapour in arc welding, *J. Phys. Appl. Phys.* 43 (43) (2010) 434001.
- [40] S.C. Chou, M. Trask, J. Danovitch, X.L. Wang, J.P. Choi, M. Brochu, Pulsed laser powder bed fusion additive manufacturing of A356, *Mater. Char.* 143 (2018) 27–33.
- [41] A.G. Demir, L. Mazzoleni, L. Caprio, M. Pacher, B. Previtali, Complementary use of pulsed and continuous wave emission modes to stabilize melt pool geometry in laser powder bed fusion, *Opt Laser. Technol.* 113 (2019) 15–26.
- [42] K. Georgilas, R.H.U. Khan, M.E. Kartal, The influence of pulsed laser powder bed fusion process parameters on Inconel 718 material properties, *Mater. Sci. Eng., A* 769 (2020) 138527.
- [43] M. Zavala-Arredondo, et al., Use of power factor and specific point energy as design parameters in laser powder-bed-fusion (L-PBF) of AlSi10Mg alloy, *Mater. Des.* 182 (2019) 108018.